

ABSTRACT

Title of dissertation: **CONTROL, DYNAMICS, AND EPIDEMIC
SPREADING IN COMPLEX SYSTEMS**

Viktor Nagy, Doctor of Philosophy, 2009

Dissertation directed by: **Professor Edward Ott
Department of Physics**

In this thesis we investigate three problems involving the control and dynamics of complex systems.

(a) We first address the problem of controlling spatiotemporally chaotic systems using a forecast-based feedback control technique. As an example, we suppress turbulent spikes in simulations of the two-dimensional complex Ginzburg-Landau equation in the limit of small dissipation.

(b) In our second problem we examine the dynamical evolution of the one-dimensional self-organized forest fire model, when the system is far from its statistically steady-state. In particular, we investigate situations in which conditions change on a time-scale that is faster than, or of the order of the typical system relaxation time.

(c) Finally, we provide a mean field theory for a discrete time-step model of epidemic spreading on uncorrelated networks. The effect of degree distribution, time delays, and infection rate on the stability of oscillating and fixed point solutions is examined through analysis of discrete time mean-field equations.

CONTROL, DYNAMICS, AND EPIDEMIC
SPREADING IN COMPLEX SYSTEMS

by

Viktor Nagy

Dissertation submitted to the Faculty of the Graduate School of the
University of Maryland, College Park in partial fulfillment
of the requirements for the degree of
Doctor of Philosophy
2009

Advisory Committee:
Professor Edward Ott, Chair/Advisor
Professor Brian Hunt
Professor Michelle Girvan
Professor Rajarshi Roy
Professor Thomas Antonsen

Dedication

To my wife Zsofi and to my parents

Acknowledgments

There are many people to whom I am grateful for making my journey through graduate school possible.

First of all, I would like to thank my wife Zsofi for the invaluable help she gave me throughout the years. She was my most faithful supporter and helped me to become an independent, self confident person. Without her wisdom I would not have been able to overcome the hardships. She listened to me with patience and compassion, and was happier for my success than I myself.

I was very fortunate to have Professor Edward Ott as my advisor. I am grateful for his guidance and for the tremendous effort he made to turn me into a better scientist. Thanks to him, I learned that even the greatest scientific ideas are lost if not conveyed in a clear accessible manner. He is the sharpest minded critic, passionate about perfection, who helped me to become a better writer, a confident speaker, invaluable qualities for which I will be grateful for the rest of my career. He was always willing to take on interesting projects, and working with him was both intellectually rewarding and inspiring. I am convinced that the greatest reward for him to see his students succeed.

I met many wonderful people at Maryland. I would like to thank Francesco Sorrentino, my friend, for his support, encouragement, and fruitful scientific discussions. I would like to thank the Maryland Chaos group for creating such a friendly environment: Nick Mecholsky, Seung-Jong Baek, Matthew Cornick, and James Hart.

Within the staff in the Physics Department are some of the nicest people I ever met. I am particularly grateful for the kindness and professionalism of Jane Hessing.

Finally, I would like to thank my parents for their encouragement and support.

Table of Contents

List of Figures	vii
1 Introduction	1
2 Control of Rare Intense Events in Spatiotemporally Chaotic Systems	4
2.1 Introduction	4
2.2 The Complex Ginzburg-Landau Equation as a Model for Rare Intense Events	7
2.3 Perfect Control Scenario	12
2.3.1 Control Strategy	14
2.3.2 Numerical Experiments	18
2.3.3 Dependence on the Control Parameters m, u_c	22
2.4 Imperfect control Scenario	25
2.4.1 Imperfect model	25
2.4.2 Imperfect state estimation	27
2.5 Conclusion	28
3 Dynamics of a one dimensional self-organized model	32
3.1 Introduction	32
3.2 Dynamics of the forest-fire model in one dimension	36
3.2.1 Framework	36
3.2.2 Continuous time approximation	39
3.2.3 Estimation of $P_2(a, b; t)$	41
3.3 Numerical experiments	47
3.3.1 Relaxation time	47
3.3.2 Accuracy of our approximate descriptions of FFM dynamics	48
3.3.3 Cluster-size dependent dynamics	52
3.3.4 Dynamics for time dependent $\gamma(t)$	54
3.4 Conclusion	57
4 Mean-field theory of a recurrent epidemiological model	61
4.1 Introduction	61
4.2 Framework	64
4.3 Linear contagion scheme	69
4.3.1 Fixed Points	69
4.3.2 Shur Stability	71
4.3.3 Phase Diagram	73
4.4 Nonlinear scheme	75
4.4.1 Fixed Points	76
4.4.2 Stability	78
4.5 Numerical results for fixed network structure	83
4.5.1 Linear Contagion	83
4.5.2 Nonlinear Contagion	85

4.6	Conclusion	89
4.7	Appendix A	90
4.8	Appendix B	90
4.9	Appendix C	91
	Bibliography	93

List of Figures

2.1	3D view of a CGL burst.	9
2.2	$ u _{max}$ versus time for an individual burst. Solution of Eq. (2.1) with parameters as given in (2.2).	10
2.3	U_{max} versus time for Eq. (2.1) with periodic boundary conditions on a square with sidelength $l = 60$	11
2.4	$P(v)$ and $\ln(P(v))$ versus v . The distributions are calculated using a computer experiment of duration $t = 40$ for Eq. (2.1) with parameters as given in (2.2) (# of bursts with $(u _{max} \geq 1) \simeq 5000$).	13
2.5	Systematic illustration of the control procedure.	16
2.6	Systematic illustration of the control procedure.	17
2.7	U_{max} versus time without control (dotted curve) and with control (solid curve) using the standard control parameters given in (2.12).	21
2.8	$\ln(P(v))$ versus v for $m = 0, 1/32, 1/16, 1/8, 1/4, 1/2$ with $u_c = u_c^{sd}$	22
2.9	Expense of control $\ln(\delta)$ as a function of $\ln(m)$ with $u_c = u_c^{sd}$	23
2.10	$\ln(U(P_0))$ versus $\ln(m)$ with $u_c = u_c^{sd}$	24
2.11	$\ln(\delta)$ versus u_c with $m = m^{sd}$	24
2.12	Comparison of perfect and imperfect model scenarios.	26
2.13	Comparison of $P(v)$ for the standard control parameters (2.12) for different observation densities, with $\rho = l/512, l/32, l/16$	29
2.14	Comparison of $P(v)$ for the standard control parameters (2.12) for different noise levels ϵ with $\rho = l/512$ and $\rho = l/32$	29
3.1	A state of the FFM for $L = 32$	37
3.2	S_{10}/L versus time t for $\gamma = 5 \times 10^{-3}$ and $L = 10^6$ with empty grid initial conditions. The dash-dotted curve is the result from a full numerical simulation, while the solid curve is from the solution of (3.14) and (3.17).	42
3.3	2-clusters are created by coalescing 3-cluster configurations.	43

3.4	Difference between the perturbed and time-asymptotic distributions for different initial conditions with $\gamma = 5 \times 10^{-3}$ and $L = 10^6$	48
3.5	The accuracy parameter Δ versus time with $L = 10^6$ and $\gamma = 5 \times 10^{-2}, 5 \times 10^{-3}, 2 \times 10^{-3}$ for the second-order approximation (3.19) and (3.20).	49
3.6	The accuracy parameter Δ_∞ versus the forest-fire intensity γ , for the second-order model given by (3.19) and (3.20) (solid curve) and for the first-order model given by (3.17) (dashed curve). $L = 10^6$	50
3.7	S_{10} versus time t for $\gamma = 5 \times 10^{-3}$ and $L = 10^6$ with empty grid initial conditions. The dotted curves are the results from a full numerical simulation of the FFM, while the solid curves in (a) and (b) correspond respectively to the first and second-order approximation.	50
3.8	The time-asymptotic $\ln(S_x)$ versus $\ln(x)$. The dotted curve is the result from a full numerical simulation of the FFM, while the solid curve is from the second-order approximation. The parameter values are $\gamma = 5 \times 10^{-3}$, $L = 10^6$	51
3.9	S_x versus time t for $\gamma = 5 \times 10^{-3}$, $L = 10^6$, and $x = 10, 14, 18, 26$ for the second-order approximation with empty grid initial conditions.	52
3.10	$t_{max}(x)$ versus x for $\gamma = 5 \times 10^{-3}$, $L = 10^6$. The dots are the results from a full numerical simulation of the FFM, while the solid curve is the analytical result from the first-order approximation, i.e., $t_{max}(x) = \ln(x/2 + 1)$ (Eq. (4.47)).	53
3.11	S_{10}/L versus t for $\gamma_0 = 5 \times 10^{-3}$, $L = 10^6$, $\omega = 1$, and $A = 0.5$. The dotted curve is the result from the FFM, while the solid curve is from the second-order approximation.	54
3.12	The amplitude of oscillation $a(x)$ versus the cluster size x for $\gamma_0 = 5 \times 10^{-3}$, $L = 10^6$, $\omega = 1$, and $A = 0.5$	55
3.13	$\Delta\phi(x)$ versus x . The solid curve is for the second-order approximation, dots correspond to the full FFM. Parameter values are $\gamma = 5 \times 10^{-3}$, $L = 10^6$, $\omega = 1$, and $A = 0.5$	59
3.14	$a(1)/L$ versus ω for the second-order approximation ($\omega_0 \approx 1.14$). Parameter values are $\gamma = 5 \times 10^{-3}$, $L = 10^6$, and $A = 0.5$	59
3.15	$\Delta\phi(x)$ versus x for the second-order approximation. Parameter values are $\gamma_0 = 5 \times 10^{-3}$, $L = 10^6$, $\omega = 1, 2, 4$, and $A = 0.5$	60

3.16	S_{10} versus S_6 for $\gamma_0 = 5 \times 10^{-3}$, $L = 10^6$, $\omega = 1$, and $A = 0.5$ for the second order approximation (a) and the FFM (b). The dotted curve in (b) corresponds to the second order approximation.	60
4.1	Stability regions for Eq.(4.21) for $\tau_I = 2$ and $\tau_R = 2$. The straight line starting from point $(a, b) = (1/\tau_I, 0)$ corresponds to the equation $a\tau_I + b(\tau_I + \tau_R) = 1$, while the curve is given by Eqs. (4.22) and (4.23).	73
4.2	Approximation of the border of stability region with a tangent starting at point (a_0, b_0) , for $\tau_I = 2$ and $\tau_R = 2$	74
4.3	Phase portrait of Eq.(4.10) with $\tau_I = 4$. The solid curve separating oscillatory and prevalent solutions is obtained from full numerical solution of Eq.(4.10), while the dotted curve is given by (4.24).	75
4.4	Solution of the fixed point problem $x = f(x)$, where $f(x)$ is given by Eq.(4.26).	77
4.5	Stability regions for the nonlinear scheme as a function of τ_R and infection probability μ for $\tau_I = 2$. Results for the full numerical simulation (solid curve) are compared to the approximation corresponding to Eq. (4.41) (dashed curve) for the degree distribution $P_k = \delta_{k,10}$	81
4.6	Stability regions for nonlinear contagion obtained from full numerical solution of Eqs.(4.31), with $P_k \sim k^{-\gamma}$, $\tau_I = 4$, and $\tau_R = 2$	81
4.7	Comparison of experimental results of σ with distributions $P_k \sim e^{-0.1k}$ and $P_k \sim k^{-3}$ for $\tau_I = 4$, $\tau_R = 7$, and $N = 1.5 \times 10^4$. (Linear contagion)	86
4.8	Comparison of experimental (dashed curve) and mean-field results (4.13-4.14) (continuous curve) for the fraction of infected individuals (I) for $\tau_I = 4$, $\tau_R = 4$, $P_k \sim e^{-0.1k}$, and $N = 1.5 \times 10^4$. (Linear contagion)	86
4.9	Comparison of mean-field results (4.24) (continuous curve) with experimental results for the Neimark-bifurcation point μ_1 as function of τ_R for the distributions $P_k = \delta_{k,15}$ (dashed curve) and $P_k = \delta_{k,10}$ (dotted curve) for $\tau_I = 4$ and $N = 1.5 \times 10^4$.(Linear contagion)	87
4.10	Comparison of experimental (dashed curve) and mean-field results (4.30) (continuous curve) for the fraction of infected individuals (I), for $\tau_I = 1$, $\tau_R = 4$, $P_k \sim k^{-4}$, and $N = 1.5 \times 10^4$.(Nonlinear contagion)	87

4.11 Comparison of mean-field results (4.24) (continuous curve) with experimental results (dashed curve) for the Neimark-bifurcation point μ_1 as function of τ_R . $P_k \sim k^{-4}$, $\tau_I = 2$, $\tau_R = 4$ and $N = 1.5 \times 10^4$. (Nonlinear case)	88
4.12 Experimental results for the for the Neimark-bifurcation point μ_1 , for $P_k \sim k^{-\gamma}$ as function of the exponent γ , $\tau_I = 4$, $\tau_R = 2$, and $N = 2 \times 10^4$	88

Chapter 1

Introduction

The study of complex systems has become increasingly important and active in many scientific disciplines, partly because of its broad range of potential applications. In this thesis we examine the control and dynamics of a variety of complex systems.

In Chapter 2 we address the problem of using feedback control for the purpose of suppressing unwanted rare intense events in spatially extended systems. As an example, we investigate the use of control to suppress turbulent spikes in simulations of the two-dimensional complex Ginzburg-Landau equation in the limit of small dissipation. We explore how information obtained by forecasting can be used to implement spatially and temporally localized control parameter changes and how control strength and cost are related to effectiveness in this framework. The effects of model error and imperfect state measurement are also considered. The main advantage of our approach is that it requires very small changes in the control parameters to achieve the desired effect. Our purpose is to eliminate the potentially harmful part of spatiotemporal chaos, rather than eliminating chaos itself, making the method particularly suitable for potential applications e.g., weather control.

In the remaining two Chapters we study the behavior of systems defined by cellular automata. In cellular-automata-based models simple dynamical rules can

result in very complicated and potentially meaningful global behavior, illustrating that complex global behavior does not necessarily require complicated rules as building blocks.

In Chapter 3 we examine the dynamical evolution of the one-dimensional self-organized forest fire model (FFM), when the system is far from its statistically steady-state. In particular, we investigate situations in which external conditions change on a time-scale that is faster than, or of the order of the typical time needed for relaxation. An analytical approach is introduced based on a hierarchy of first-order nonlinear differential equations. This hierarchy can be closed at any level, yielding a sequence of successively more accurate descriptions of the dynamics. It is found that our approximate description can yield a faithful description of the FFM dynamics, even when a low order truncation is used. Employing both full simulations of the FFM and our approximate descriptions, we examine the time scales and cluster-size-dependent dynamics of relaxation to the statistical equilibrium. As an example of changing external conditions in a natural forest, the effects of a time-dependent lightning frequency are considered.

Finally, in Chapter 4 we examine properties of disease spreading on uncorrelated networks. In particular, we provide a mean field theory for the discrete time-step SIRS (Susceptible, Infected, Recovered, Susceptible) model on uncorrelated networks with arbitrary degree distributions. The effect of network structure, time delays, and infection rate on the stability of oscillating and fixed point solutions is examined through analysis of discrete time, mean field equations. Consideration of two scenarios for disease contagion demonstrates that the manner in which conta-

gion is transmitted from an infected individual to a contacted susceptible individual is of primary importance. In particular, the manner of contagion transmission determines how the degree distribution affects model behavior. We find excellent agreement between our theoretical results and numerical simulations on networks with large average connectivity.

The thesis is based on the following publications:

- Chapter 2: V. Nagy and E. Ott, *Control of rare intense events in spatiotemporally chaotic systems*, Phys. Rev. E 066206 **76** (2007)
- Chapter 3: V. Nagy and E. Ott, *Dynamics of the one-dimensional self-organized forest fire model*, Phys. Rev. E 021113 **78** (2008)
- Chapter 4: V. Nagy, *Mean-field theory of a recurrent epidemiological model*, submitted to Phys. Rev. E (2009)

Chapter 2

Control of Rare Intense Events in Spatiotemporally Chaotic Systems

2.1 Introduction

There are numerous examples of rare intense events in spatiotemporal chaotic systems [1], some of which have great practical importance. Atmospheric events like tornados and hurricanes can be particularly harmful and capable of causing serious loss. Another example is the occurrence of large height ocean waves [2] (so-called rogue waves). An example of a nicely controllable laboratory model exhibiting rare intense event behavior is that of parametrically forced surface waves on water which intermittently produce high amplitude spatially localized upward jetting [3]. For cases in which such intense events are destructive, it would be highly desirable to find effective methods for suppressing them.

Synchronization and control of spatially extended systems has attracted considerable attention during the last two decades partly because of the broad range of its potential applications, e.g, [4, 5, 6, 7]. The first approaches to control spatiotemporal chaos were extensions of the algorithm in Ref. [8]. Subsequently Pyragas suggested a delayed continuous feedback control method [9] which was extended to spatiotemporal systems to suppress turbulence in the complex Ginzburg-Landau equation [4] and to control chaos in an optical system by Lu *et al.*[6]. As simple models for spatially extended systems, coupled map lattice systems have attracted

considerable attention where so-called ‘pinning control’ techniques have been investigated [10, 11]. In the context of low dimensional chaos, control for the suppression of rare intense events (e.g., associated with parameters putting the system slightly past a ‘crisis’ [12]) has been addressed in Refs. [13].

Our purpose is to address the problem of controlling rare intense events in spatiotemporally chaotic systems. We often refer to such rare intense events as ‘bursts’. We take an approach in which we first forecast the future occurrence of an unwanted burst event in the uncontrolled system. We then use this information for planning a control to eliminate this burst event. We summarize the requirements of our control set-up as follows:

- A good model of the system dynamics.
- Measurements of the state of the system.
- A means of using the previous two to predict the future system state and in particular the occurrence of bursts.
- Available control variables that can be physically changed to influence the system evolution.
- A strategy for deciding how to program these control variables.

Thus our considerations here are not applicable to examples of rare intense events (e.g., earthquakes) where the system is so complex that reliable prediction has so far proved unattainable. On the other hand, weather and hurricane prediction

is rapidly advancing and may, in the future, provide an example, where our considerations are of interest. For the case of hurricanes, one possibility [14] is to deposit surfactant on the ocean surface in the region of an incipient hurricane to reduce the evaporation that powers the storm. Our purpose is to illustrate and examine the feasibility and limitations of burst elimination control for appropriate spatio-temporally chaotic systems. For this purpose we employ a specific simple model which will allow us to address many of the more basic issues raised by the above program. In particular, we use as our basic model system the complex Ginzburg-Landau (CGL) equation with parameter values chosen so that the equation exhibits large spatially and temporally localized bursts that occur in a highly intermittent manner.

As background, in Sec. 2.2 we discuss the properties of the uncontrolled CGL equation in the regime of interest. In Sec. 2.3 we consider a ‘perfect scenario’ in which it is assumed that the following conditions hold:

- We are able to exactly sense the entire system state.
- We are in possession of an exact model for the system being controlled and we can integrate this model with arbitrarily fine precision.

By examining this ‘perfect scenario’ we are able to address several issues illustrating the best possible results that could be expected. For example, how far do we need to predict into the future, and how does this prediction horizon influence the size and strength of the needed control? Can controls of fairly small size, if strategically applied and programmed, eliminate large, potentially catastrophic events? Can

the control to eliminate a spatially localized burst itself be localized in space and time? We find that potentially favorable results can often be obtained. Thus the results from our ‘perfect scenario’ tests motivate further study to investigate non-ideal effects. This will be done in Sec. 2.4 in which we consider the effects of the following practically important factors.

- Estimation of the current system state from *noisy* observations at a *finite* number of spatial locations.
- Model error (i.e., the model used to forecast bursts does not precisely correspond to the true dynamics of the system to be controlled).

In Sec. 2.5 we summarize our conclusions.

2.2 The Complex Ginzburg-Landau Equation as a Model for Rare Intense Events

The Complex Ginzburg-Landau (CGL) equation,

$$\partial_t u = Ru - (\gamma - i\alpha)|u|^2 u + (\mu + i\beta)\nabla^2 u, \quad (2.1)$$

is a generic amplitude equation that describes the slow modulation of physical fields in space and time near the threshold of an instability (e.g., see Ref. [15]). It has been studied as a model for such diverse situations as fluid dynamics (Rayleigh-Bernard convection[16], Taylor-Couette flow [17] and Poiseuille flow [18]), and nonlinear chemical oscillation [19]. The CGL equation can also be viewed as a dissipative extension of the nonlinear Schrodinger (NLS) equation which corresponds to Eq.

(2.1) with R, γ and μ set to zero. For real positive $(R, \gamma, \alpha, \mu, \beta)$ solutions of the CGL equation are global in time [20, 21], while, in contrast, the NLS equation can exhibit finite-time singularities in which the field approaches infinity (‘blow-up’) at some point in space as the time approaches a singularity time from below [23, 24, 25]. Here we consider the CGL equation on a two dimensional domain (denoted Ω) with periodic boundary conditions. Furthermore, we consider a parameter region where the CGL equation is close the NLS limit:

$$\alpha = \beta = 40 \gg \gamma = R = \mu = 1 \tag{2.2}$$

In this regime the CGL solution intermittently develops high-amplitude, spatially localized, intense bursts [26, 27, 28] which can be considered as dissipative versions of the finite-time blow-up solutions of the NLS equation. Due to dissipation (nonzero γ and μ) the amplitude of these CGL bursts (in contrast to the NLS blow-up solutions) never reaches infinity [20, 21]. We consider such CGL bursts as a generic model for rare intense events.

In our numerical solution of Eq. (2.1) we employ periodic boundary conditions on a square with sidelength $l = 60$. We use a 512×512 grid and a second-order accurate operator splitting method in time (e.g., Ref. [22]) with adaptively changing time-step. The accuracy of our numerical simulations is most restricted by the limited spatial resolution as bursts exhibit large amplitude variations within small distances. In order to check the accuracy of the selected method, we performed our numerical integration for finer resolutions in space and time and found good quantitative agreement between the results.

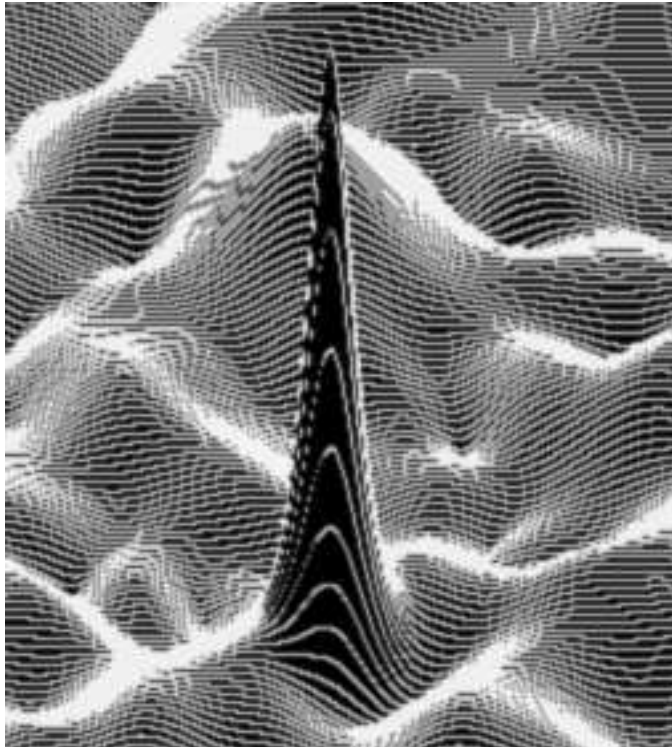


Figure 2.1: 3D view of a CGL burst.

We start our numerical integration from random initial conditions and integrate the system forward in time until transients related to the initial conditions seem to be absent (i.e., the solution approaches the compact global attractor [21]). We use the resulting state (labeled $t = 0$) as an initial condition for the following calculations. Figure 2.1 shows a snapshot of the spatial dependence of $|u|$ in a region containing a burst at the snapshot time. Figure 2.2 shows $|u|$ evaluated at the spatial location of the maximum of $|u|$ in Fig.2.1 versus time. As seen in Fig.2.2, this quantity initially fluctuates showing both increasing and decreasing behavior. Subsequently, when conditions are favorable to lead to formation of a burst, the amplitude starts to increase rapidly. When bursts finally reach their maximum amplitude, to within a good approximation, they are circularly symmetric around their

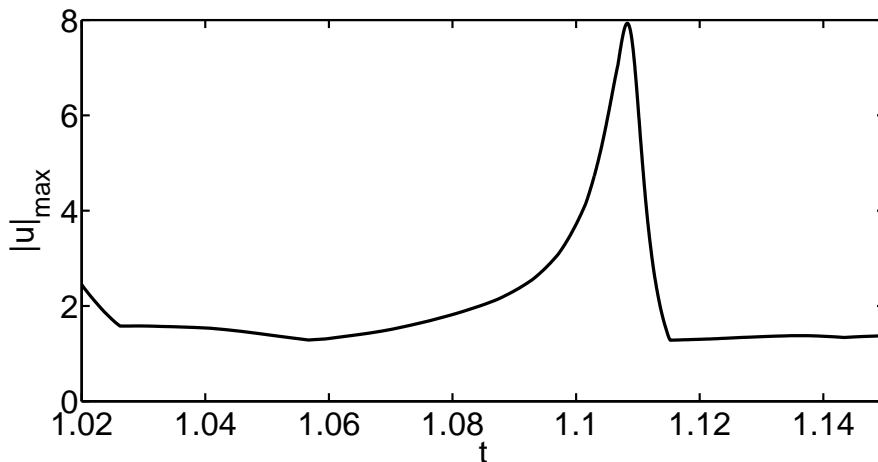


Figure 2.2: $|u|_{max}$ versus time for an individual burst. Solution of Eq. (2.1) with parameters as given in (2.2).

maxima and differ only in an appropriate scaling,

$$\frac{u'(r/|u'|_{max})}{|u'|_{max}} \simeq \frac{u(r/|u|_{max})}{|u|_{max}} e^{i\phi}, \quad (2.3)$$

where $u(r)$ and $u'(r)$ denote solutions of a CGL equation at the time where two independent bursts reach their amplitude, with r denoting the spatial distance from the burst maximum. Self similarity first appears close to the spatial location of the maximum amplitude and, as the increase continues, extends to larger r . Thus, despite the complexity of the underlying system, we have to control objects that are becoming quite similar as they approach their maximum amplitudes. The observed approximate similarity of CGL bursts is inherited from the the well-studied asymptotic self-similarity of the blow-up solutions of the NLS equation [29, 30, 31].

Figure 2.3 shows the global spatial maximum of the amplitude,

$$U_{max} = \max_{x \in \Omega} |u(x, t)|, \quad (2.4)$$

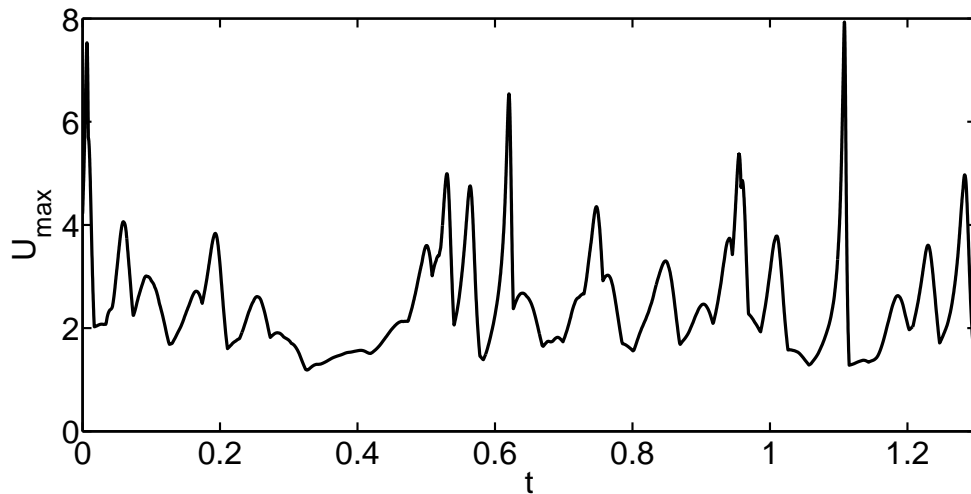


Figure 2.3: U_{max} versus time for Eq. (2.1) with periodic boundary conditions on a square with sidelength $l = 60$.

as a function of time resulting from a typical numerical integration of (2.1) with parameters (2.2).

We note that for this simulation the spatially averaged amplitude over the periodic area Ω ,

$$U_{av}(t) = \frac{1}{|\Omega|} \int_{\Omega} |u(x, t)| d^2x, \quad (2.5)$$

is about $U_{av} \simeq 0.3$ and fluctuates less than 10% with time. This average amplitude of ~ 0.3 is to be contrasted with the much larger values sometimes attained by $U_{max}(t)$; e.g., the largest U_{max} in Fig.2.3 is $U_{max} \simeq 7.5$, and an integration somewhat longer yields a value of U_{max} above 13. Bursting also occurs on a very fast timescale; the usual time needed for a burst to develop from $|u| = 1$ to $|u|_{max}$ is typically smaller than 0.1. Integrating the solution for a sufficiency long time, we can determine the

conditional empirical probability $P(v)$ of maximum burst amplitudes,

$$P(v) = \frac{\# \text{ of bursts with } (|u|_{max} \geq v)}{\# \text{ of bursts with } (|u|_{max} \geq 1)}, \quad (2.6)$$

Thus, we consider the distribution only for those bursts whose maximum amplitude exceeds 1. $P(v)$ is shown in Fig. 2.4(a), and it illustrates that, although extremely high amplitudes occur frequently, because of their fast timescale, their contribution to the distribution is relatively small. As we will discuss later, these large amplitude bursts make a significant contribution to the overall average dissipation in the system. Figure 2.4(b) shows a log-linear plot of the same data as in Fig. 2.4(a). From its approximately linear form we see that $P(x) \sim \exp(-cx)$ for $x \in [2, 10]$, i.e., $P(v)$ has an exponential event tail. For further details on statistics of the CGL equation see [26, 32]. The characteristics of CGL bursts seen in Figs. 2.1-2.4 make them particularly suitable as a model for rare intense events in spatiotemporally chaotic systems.

2.3 Perfect Control Scenario

We assume that in real physical situations the most violent rare events are of primary concern. Thus, in our model experiments using the CGL equation our intention is to deal with the highest amplitude bursts. We choose an amplitude u_c past which we assume a burst becomes particularly destructive. Thus we wish our control to prevent bursts of amplitude larger than u_c , which we suppose to be much larger than the average amplitude, $u_c \gg U_{ave}$. We refer to u_c as the *control limit*.

Assume that at any given time t_0 we have an estimate of the system state

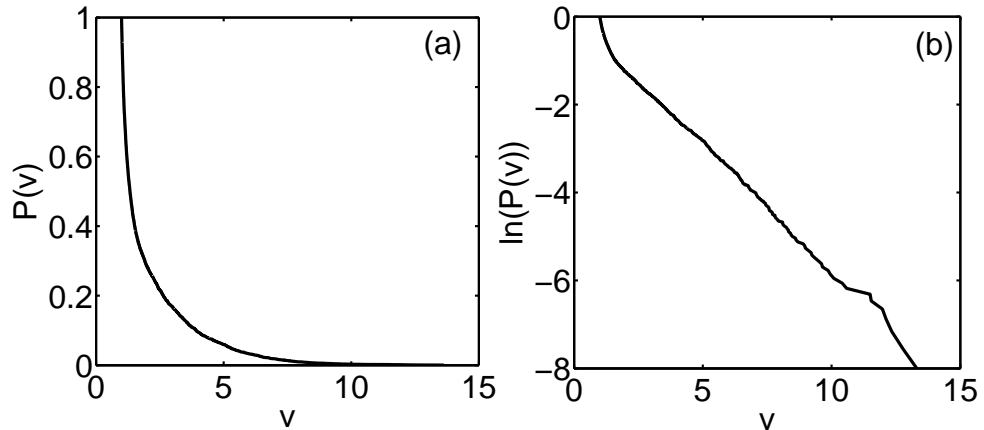


Figure 2.4: $P(v)$ and $\ln(P(v))$ versus v . The distributions are calculated using a computer experiment of duration $t = 40$ for Eq. (2.1) with parameters as given in (2.2) (# of bursts with $(|u|_{max} \geq 1) \simeq 5000$).

$u_e(x, t_0)$ and a model M'_τ for advancing the uncontrolled system state forward in time by the amount τ . Then our forecast is:

$$u_f(x, t) = M'_\tau [u_e(x, t_0)], \quad t > t_0 \quad (2.7)$$

We note that in general $u_e(x, t_0)$ may differ from the true system state $u(x, t_0)$, (i.e., $|u_e(x, t_0) - u(x, t_0)| > 0$), and M'_τ may differ from the true system dynamics, M_τ , (i.e., $|M'_\tau [u(x, t_0)] - M_\tau [u(x, t_0)]| > 0$). In the ideal case, or ‘perfect scenario’, we assume that such differences are absent. In particular $u(x, t_0) = u_e(x, t_0)$, and $M_\tau = M'_\tau$, where M_τ and M'_τ are integrations of (2.1) using the same numerical algorithms (including space and time gridding) for both M_τ and M'_τ . (In Sec. 2.4 we consider what happens when these ideal conditions do not hold.)

2.3.1 Control Strategy

We introduce the following definitions:

- Let $C_r(x)$ be the circular region in the doubly periodic domain Ω that is within a distance r of the point x ,

$$C_r(x) = \{\text{the set of } y \text{ for which } |(y - x) \text{ modulo } l| < r\}, \quad (2.8)$$

where l is the periodicity length.

- Define a *burst* b as a local space-time maximum of $|u|$ that satisfies $|u| > u_c$ and denote its coordinates by (x_b, t_b) , where x_b and t_b are the spatial location and time of burst b .
- Define *cycle times* $t_n = t_0 + n\Delta T$, where t_0 is the time at which we start our control procedure, n is a positive integer, and ΔT is a fixed time interval.
- Define a list L of burst coordinates.
- The act of making a forecast is defined as taking an estimate of the current state of the system, integrating a copy of this current state forward in time via a forecasting system model, and monitoring the result.

Our control procedure is as follows.

1. Start with $n = 0$ and the list L empty.
2. At time t_n estimate the current state of the system to be controlled.

3. Using the state estimate $u_e(x, t_n)$ obtained in step 2, do a forecast to determine the burst coordinates that occur between cycle times t_{n+1} and t_{n+2} . For the purpose of making this forecast, the forecast model is integrated with control applied at (x, t) if x is in $C_r(x_b)$ and $t \in [t_b - \Delta T, t_b + \Delta T]$, where (x_b, t_b) is one of the entries of the list L .
4. Add the newly determined (step 3) burst coordinates to the list L .
5. As the real system (as distinct from the forecast model) evolves from the time t_n to the time t_{n+1} , apply control at those points x and times t satisfying $x \in C_r(x_b)$, $t \in [t_b - \Delta T, t_b + \Delta T]$ where (x_b, t_b) are bursts on the list L .
6. Remove burst coordinates (x_b, t_b) from the list L , if $t_b < t_{n-1}$.
7. Increase n by one and go to step 2.

We emphasize that at cycle time t_n we determine bursts in the time interval $[t_{n+1}, t_{n+2}]$ (see step 3) not in $[t_n, t_{n+1}]$. The reason why we choose sequencing this way is that we found it to be more effective compared to other types of sequencings that we have tried. A reason for this that control, particularly if it is limited in strength, needs a sufficient amount of time to take effect, and our setup specified above provides us with at least ΔT time units before the occurrence of a burst. (Our control algorithm also implies that there is no control between t_0 and t_1 .)

Figures 2.5 and 2.6 give a schematic illustration of the steps involving the list L and its updating. For the purpose of this schematic, we represent the two-dimensional circular region $C_r(x)$ [Eq.(2.8)] as a one dimensional interval; i.e, as

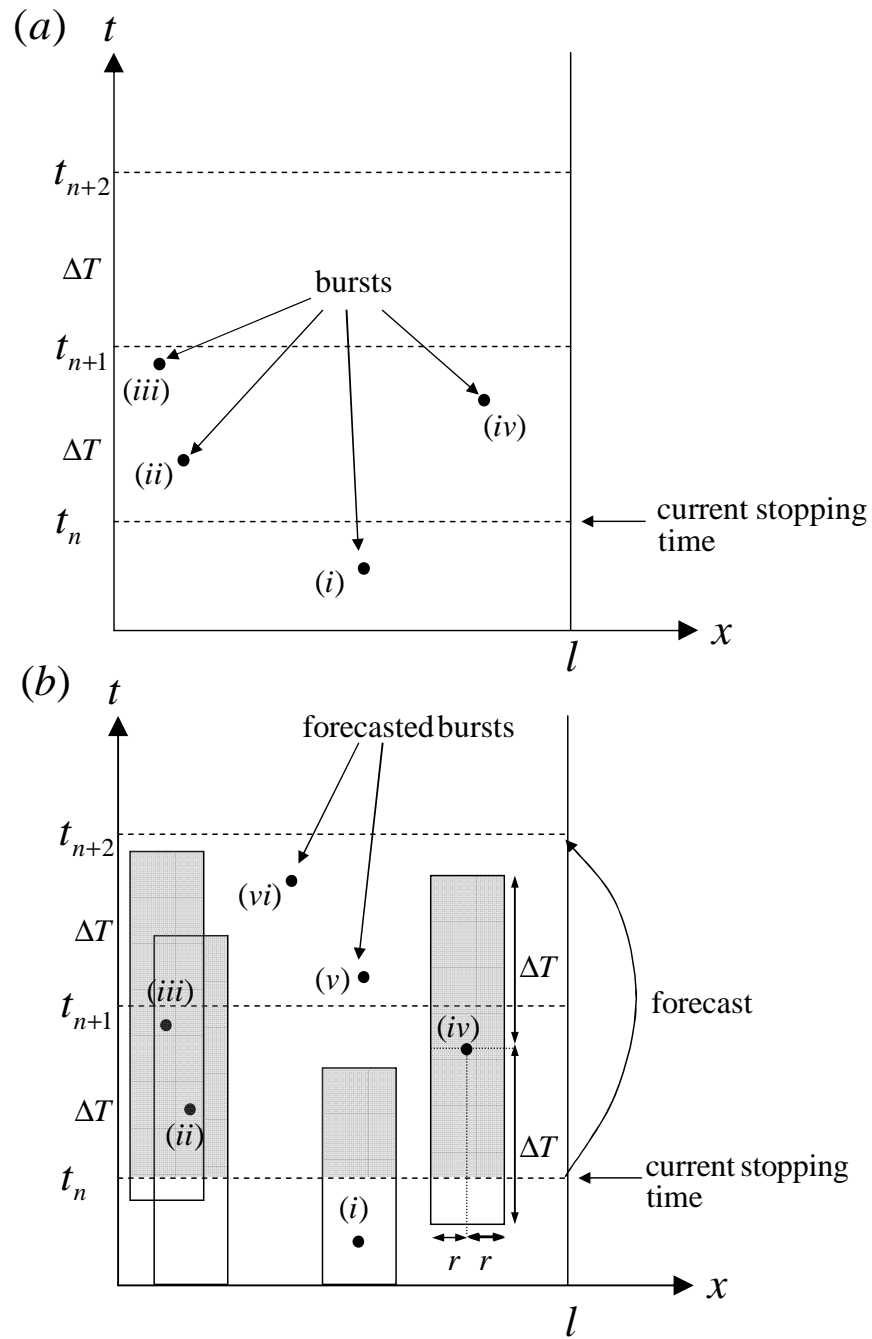


Figure 2.5: Systematic illustration of the control procedure.

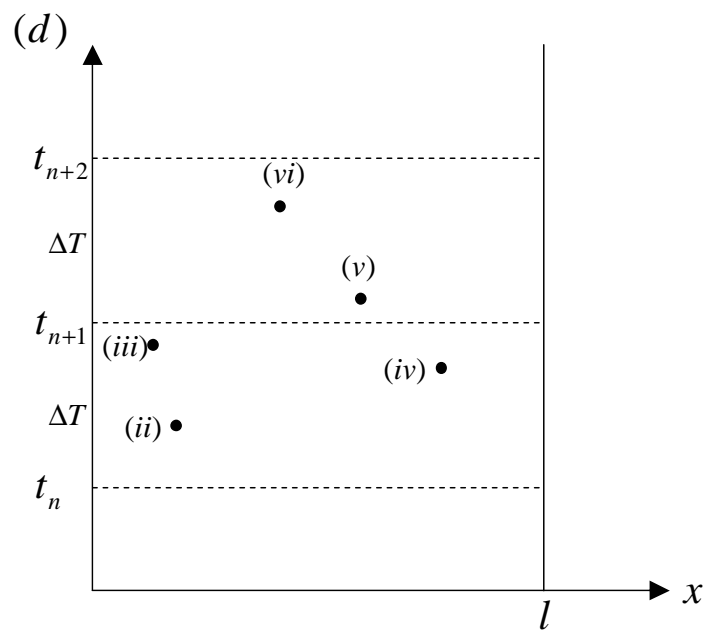
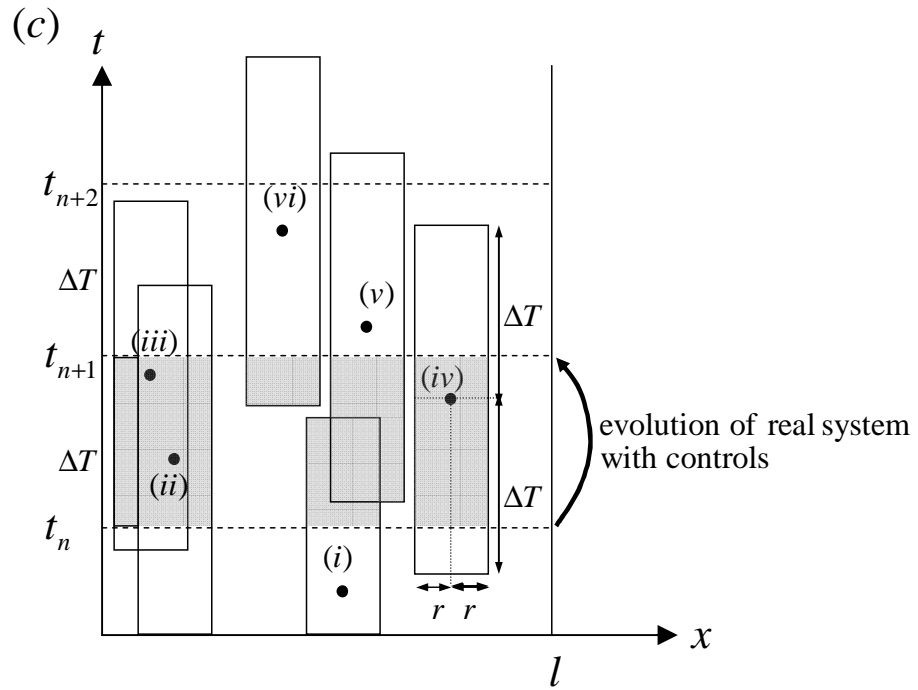


Figure 2.6: Systematic illustration of the control procedure.

$[x - r, x + r]$ where x denotes the (schematically one-dimensional) spatial location of the burst. Figure 2.5 (a) shows the situation at the end of step 7 (i.e, before application of step 2) in which the only points on the list L are those that were on the list L and whose time coordinate is greater than t_{n-1} . As illustrated in Fig. 2.5 (b), the forecast made in step 3 is done with the control applied in the shaded regions. The resulting newly forecasted bursts with $t_{n+1} \leq t_b \leq t_{n+2}$ are labeled (v) and (vi) in this figure. As illustrated in Fig. 2.6 (c), the bursts determined in step 3 (bursts (v) and (vi)) are added to the list (step 4), and the real system is controlled in the shaded region as it evolves from time t_n to time t_{n+1} (step 5). Figure 2.6 (d) shows those points that are still on the list after step 6 [in which bursts whose time coordinates smaller than t_n (labeled (i) in Figs. 2.5 and 2.6) are removed from the list].

2.3.2 Numerical Experiments

In all our numerical experiments we use the parameter α appearing in the CGL equation, Eq.(2.1), as our control variable. In a real experiment this would be analogous to assuming that there is some physical means by which α can be changed through external intervention. In particular, our control consists in lowering the value of α . That is, with reference to Fig. 2.6 (c) we replace α in Eq.2.1 by a value $\alpha' < \alpha$ for those (x, t) in the shaded region of Fig. 2.6 (c). The specific form of the control that we have chosen to implement depends on two positive parameters m, u_c . If $|u(x, t)| < 1$ for $x \in C_r(x_b)$ then we keep α unchanged. If on the other

hand, if $|u(x, t)| > 1$ for $x \in C_r(x_b)$, then we lower the value of α to α' ,

$$\alpha'(x, t) = \frac{\alpha}{1 + m(|u(x, t)| - 1)}, \text{ for } |u(x, t)| > 1, \quad (2.9)$$

$$\alpha'(x, t) = \alpha, \text{ for } |u(x, t)| \leq 1. \quad (2.10)$$

The parameter m and can be regarded as characterizing the strength of the control, with $m = 0$ corresponding to no control. Our choice is somewhat arbitrary and efficient control can also be achieved by using other choices [33].

Our spatially and temporarily localized changes in the control parameter α will modify the system dynamics, and the system consequently evolves differently than predicted in the forecast stage. This difference could conceivably lead to bursts that were not predicted during the forecast or to non-negligible changes in the timing and position of those bursts for which we already have information. This difficulty can be overcome by choosing ΔT sufficiently small that the difference due to control will not compromise our predictions. Choosing ΔT too small, however, can leave us with insufficient time to make significant changes in the amplitudes. We have found that the best selection of ΔT does not depend strongly on the particular choice of the parameters m, u_c for their tested ranges in our numerical experiments. Thus in what follows we use a constant value, namely $\Delta T = 0.1$.

Considering the entire periodic box of our simulation Ω , we define the ‘expense’ of control as the fractional space-time averaged change in α :

$$\delta = \frac{1}{|\Omega|T} \int_0^T dt \int_{\Omega} \frac{|\alpha'(x, t) - \alpha|}{\alpha} d^2x, \quad (2.11)$$

where $t = 0$ corresponds to the time at which we start monitoring and controlling bursts, and $t = T$ is the time at the end of our computer experiment. We will regard

our method as effective if we can significantly lower the probability of bursts with amplitudes exceeding u_c at low expense δ . We use $r_0 = 2$, in all cases, as we have found that the results are insensitive to deviations from this value. With ΔT and r_0 fixed, we choose a ‘standard case’ for the remaining two parameters,

$$m^{sd} = 1/4, \quad u_c^{sd} = 3. \quad (2.12)$$

This ‘standard case’ serves as a point of reference for exploring the effects of varying m, u_c . In particular, we will change the value of one of the parameters, e.g, m , while fixing the other at its standard value, e.g, $u_c = u_c^{sd}$. For each such selection we determine the time averaged expense of control δ , and the empirical probability $P(v)$ ($P(v)$ is shown in Fig. 2.4 in the uncontrolled case).

We performed a series of numerical experiments where we calculate $P(v)$ using data collected from experiments with increasing durations of time $t = 20, 40, 80$ to determine the rate of convergence. We found that the results for $t = 40$ and $t = 80$ are in good agreement. Therefore we chose the time of integration to be $t = 40$ in all perfect scenario cases. Using $P_0 = 2 \times 10^{-4}$ we can also define the ‘effective largest amplitude’ that the controlled system reaches as $U(P_0)$,

$$P(U(P_0)) = P_0 \quad (2.13)$$

We numerically define this $U(P_0)$ to be the ‘effective upper limit’ of $|u|$ with our control. A typical time series of $U_{max}(t)$ versus t for a controlled run using our standard parameter set is shown in Fig. 2.7 by the full black curve. For comparison an uncontrolled run is also shown in this figure as the dotted curve. Large bursts are apparently strongly suppressed by the control. This later conclusion is also

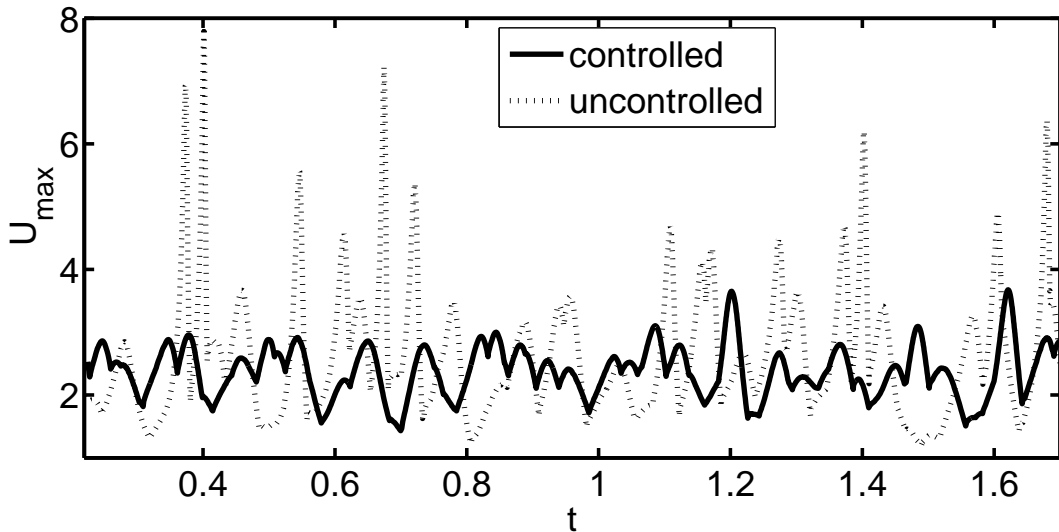


Figure 2.7: U_{max} versus time without control (dotted curve) and with control (solid curve) using the standard control parameters given in (2.12).

reflected in the substantially lower value obtained for $U(P_0)$ in the controlled case, $U(P_0) = 4.7$, as compared to $U(P_0) = 12.5$ in the uncontrolled case. It is significant that this improvement is obtained at a relatively small expense, $\delta = 2.7 \times 10^{-4}$. The reason why the control expense can be kept at such a low level is because the area where burst amplitudes exceed the control limit u_c is relatively small compared to the system size and because the burst events ($|u| > u_c$) are of short duration.

Imposing control on the system will result in its departure from its original dynamics which is accompanied by an observable quantitative change in the space-time average of $|u|^2$ denoted $\langle |u|^2 \rangle$. Starting with a long uncontrolled run and then activating our control, we observe that after the initial transients relax, the value $\langle |u|^2 \rangle$ settles down to a new level, that is somewhat *larger* than before the control was activated. We attribute this effect to the fact that the amount of dissipation in a burst event increases with its amplitude. Thus the total dissipation due to

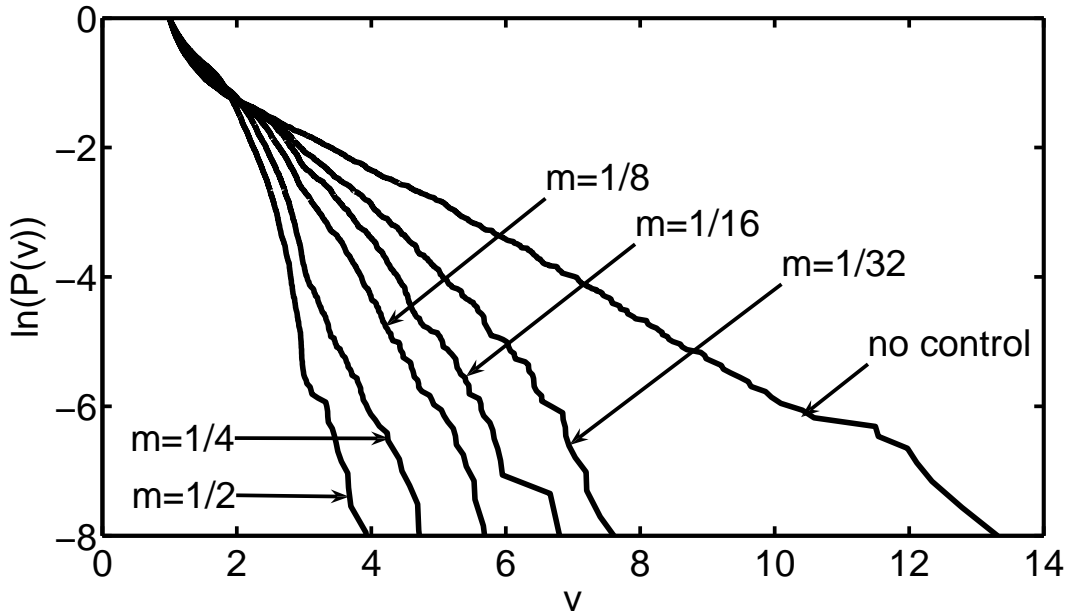


Figure 2.8: $\ln(P(v))$ versus v for $m = 0, 1/32, 1/16, 1/8, 1/4, 1/2$ with $u_c = u_c^{sd}$.

bursts can be much larger than would be expected on the basis of the relatively small fraction of the available space-time in which they are active. We believe that this lowering of the burst contribution to the space-time average dissipation is what causes the increase of $\langle |u|^2 \rangle$. With our ‘standard case’ parameter set we observed a control induced increase of $\langle |u|^2 \rangle$ from a value of 0.13 to 0.16.

2.3.3 Dependence on the Control Parameters m, u_c

A comparison of $P(v)$ for different m values is shown in Fig. 2.8. Figure 2.9 shows the expense of control δ as a function of m on a log-log plot. We can see that the dependence of δ on m is approximately a power law,

$$\delta(m) \simeq am^b \quad (2.14)$$

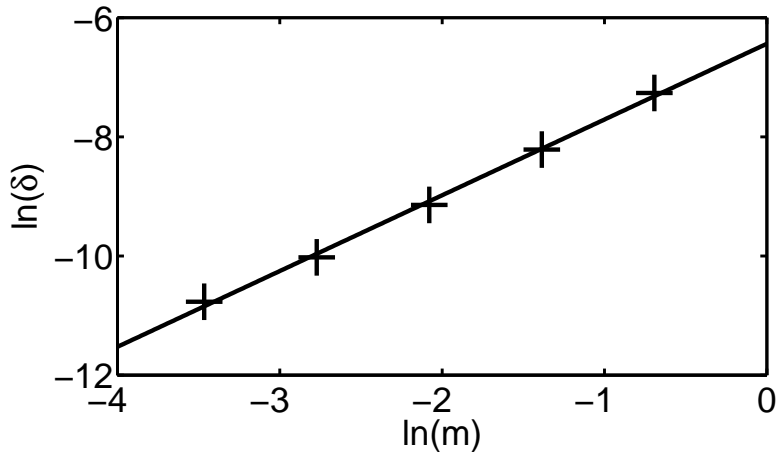


Figure 2.9: Expense of control $\ln(\delta)$ as a function of $\ln(m)$ with $u_c = u_c^{sd}$.

with $a \simeq 1.6 \times 10^{-3}$, $b \simeq 1.27$. These figures illustrate that increasing m decreases the probability of high amplitude bursts for an increasing expense δ . We also notice that, while we suppress high intensity bursts, there is an increased probability $P(v)$ for the ones whose amplitudes are below the control limit u_c . Figure 2.10 shows the the ‘effective largest amplitude’ $U(P_0)$ as a function of m on a log-log plot. The parameters of the power law dependence,

$$U(P_0) \simeq cm^{-d} \quad (2.15)$$

are $c \simeq 3.42$, $d \simeq 0.25$. As shown in Fig. 2.11 on a log-linear plot, δ has an approximately exponential dependence the on control limit u_c ,

$$\delta(u_c) \simeq ge^{-hu_c} \quad (2.16)$$

with parameters $g \simeq 1.57 \times 10^{-3}$, $h \simeq 0.6$.

Finally, in order to illustrate the benefit of our forecast driven approach, we consider what happens when we apply the control (2.9) and (2.10) everywhere and for all times (i.e., not just in the forecast-determined shaded regions of Fig. 2.4).

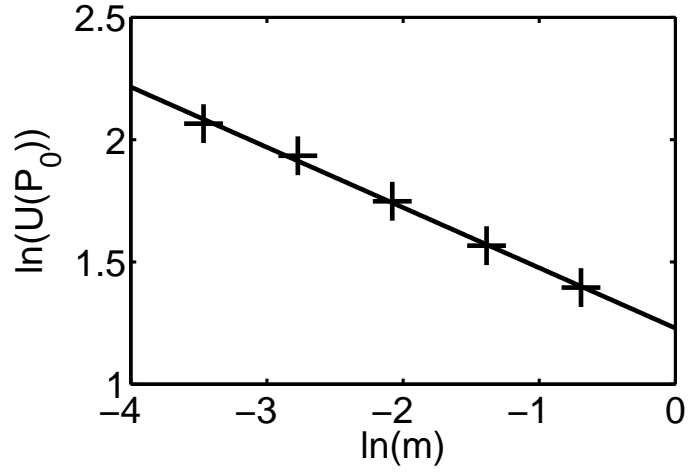


Figure 2.10: $\ln(U(P_0))$ versus $\ln(m)$ with $u_c = u_c^{sd}$.

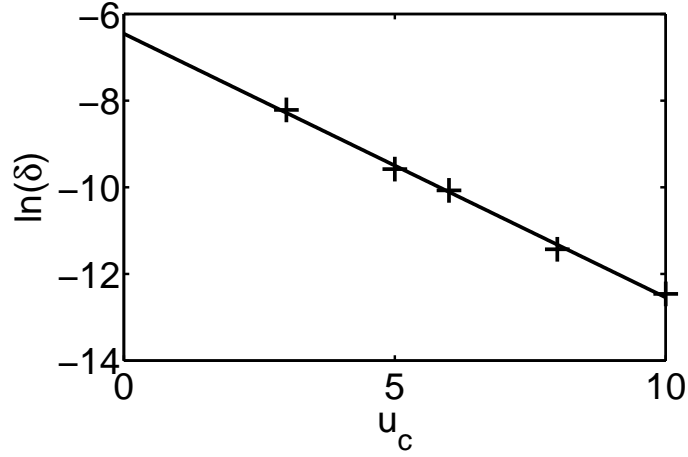


Figure 2.11: $\ln(\delta)$ versus u_c with $m = m^{sd}$.

Generally, we find that to achieve a similar level of burst suppression, not making use of forecasts leads to much greater cost. For example, using $m = 1/16$ and applying (2.9) for all x and t suppresses bursts with $|u|_{max} \geq 7$ at a cost $\delta \simeq 10^{-4}$. In contrast, using a forecast-based method with the parameters $m = 1/16, u_c = 7$ the cost is more than twenty times less than without forecast.

2.4 Imperfect control Scenario

In the previous section we implemented our control strategy for the case in which we possess a perfect model of the controlled system and we are able to sense the state of the system with arbitrary precision. In any real situation, however, these ideal conditions will not be met. When implementing forecasting in practice, one typically estimates the state of the system using noisy observations made at a limited number of spatial locations and makes forecast predictions using this estimate as the initial condition in the forecast model integration. In addition to the limitations imposed by the accuracy and limited number of measurements, errors in the forecast model also contribute significantly to prediction inaccuracy. If a control strategy is to be applied to practical situations, it has to show sufficient robustness under less than perfect conditions. In this section we investigate the effects both of an imperfect model and of imperfect state estimation using our standard control parameters (2.12).

2.4.1 Imperfect model

To assess the effect of using an imperfect forecasting system model we use Eq. (2.1) but with an incorrect value of the parameter β denoted β_f for our forecast model. For this purpose we will assume that we can determine the initial conditions with arbitrary precision, so that the only source of error is our imperfect model. We find that, using the imperfect forecast model in our control procedure, the maximum amplitude of bursts is rather sensitive to variations of β_f while the accuracy of the

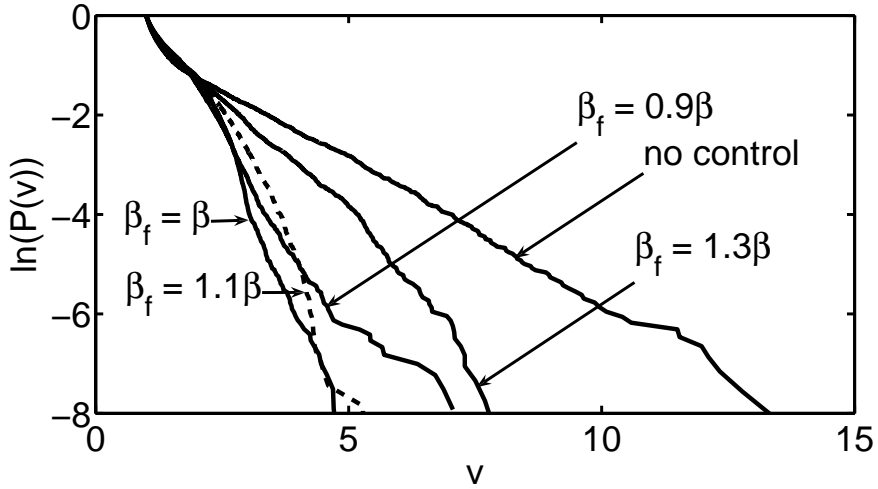


Figure 2.12: Comparison of perfect and imperfect model scenarios.

predicted burst time and location remains good. Figure 2.12 shows a comparison of $P(v)$ for the uncontrolled and controlled systems. In the controlled case we plotted the results both for the perfect $\beta_f = \beta$ and imperfect model scenarios $\beta_f = 0.9\beta, 1.1\beta, 1.3\beta$. The apparent difference in $P(v)$ between the cases $\beta_f = 1.1\beta$ and $\beta_f = 0.9\beta$ is partly due to the fact that for $\beta_f > \beta$ the predicted amplitudes are larger than for $\beta_f = \beta$ and similarly a selection of β_f below β results in a decrease of the predicted height of bursts. As a consequence, for $\beta_f < \beta$, it is more likely that the predicted amplitude is smaller than the control limit u_c and that it remains unnoticed and uncontrolled despite being above u_c in the perfect model. Our results illustrate that, in spite of substantial error in one of the parameters of Eq. (2.1), the method still delivers significant suppression of unwanted bursts at reasonably low expense: $\delta = 1.9 \times 10^{-4}$ for $\beta = 1.1\beta$ and $\delta = 3.3 \times 10^{-4}$ for $\beta = 0.9\beta$.

2.4.2 Imperfect state estimation

We implement our imperfect state estimation scenario by placing a uniformly spaced sparse square ‘observational grid’ on the entire periodic box of our simulation Ω with the observational grid points being our measuring locations. We define a measurement location density ρ as the distance between our measurement points in our observational grid (recall that our model uses a 512×512 grid on a periodic box of sidelength $l = 60$). Simulated measurements at these locations are ‘observed’ at the discrete ‘cycle times’ $t_n = t_0 + n\Delta T$, with n integer, and measurements are generated by adding noise to the ‘true’ value of u at each observation point. The noise simulates measurement error and is taken to be $\epsilon\sqrt{\langle |u|^2 \rangle_0}(r_r + ir_i)$, where $\langle |u|^2 \rangle_0$ denotes the mean squared time-space average of u in the absence of control, r_r and r_i are real, zero mean, independent, Gaussian random variables with variance one, and ϵ is a parameter characterizing the strength of the noise. We then reconstruct the system state at each ‘cycle time’ using the Whittaker-Shannon sampling theorem in two dimensions. Prerequisites for avoiding the effect of aliasing with this method are that the signal be bandlimited and that the sampling rate be at least twice the bandwidth. As observed both numerically and verified theoretically [34], at sufficiently large wavenumbers, the spatial Fourier coefficients of solutions of the CGL equation decay exponentially with increasing wavenumber. From our numerical investigations, we find that this exponential decay is also valid for the controlled system and that the assumption that the system is bandlimited is a good approximation. If we denote our sample points by $u[i, j]$, the reconstructed state

by $u(x, y)$, and the sampling grid by $G_L = \{(iL, jL) | i, j \in 0..512/L\}$, where $L = 512 \times \rho/l$, then the Whittaker-Shannon interpolation formula yields the following estimate for the reconstructed system state,

$$u(x, y) = \sum_{(i,j) \in G_L} u[i, j] \frac{\sin(\pi(x - iL)/L) \sin(\pi(y - jL)/L)}{\pi^2(x - iL)(y - jL)/L^2}.$$

We found that this approximation gives good results for $\rho = l/32$ with the exception of locations where the amplitude is large (i.e., near bursts). A significant point is that, even though $\rho = l/32$ is not fine enough to resolve high amplitude bursts, it can still be used to accurately predict such bursts. This is because the initial conditions leading to a burst are much smoother than the burst itself, and it is only such initial conditions that we need to approximate in order to make our predictions. Comparison of $P(v)$ for controlled runs with different values of the observation density ρ are shown on Fig. 2.13 for $\epsilon = 0$ (no observational noise). Results comparing the effect of different noise levels for $\rho = l/512$ and $\rho = l/32$ are shown on Fig. 2.14. Figure 2.13 indicates that the observation density $\rho = l/32$ without noise gives results that are somewhat worse than in the $\rho = l/512$ case, while $\rho = l/16$ is too sparse and gives only slight improvement over the uncontrolled system. Figure 2.14 indicates that increase of observational noise ϵ makes control increasingly less effective as shown for $\epsilon = 0.3, 0.5$.

2.5 Conclusion

We have investigated an approach to the control of rare intense events in spatiotemporally chaotic systems. The approach has several prerequisites:

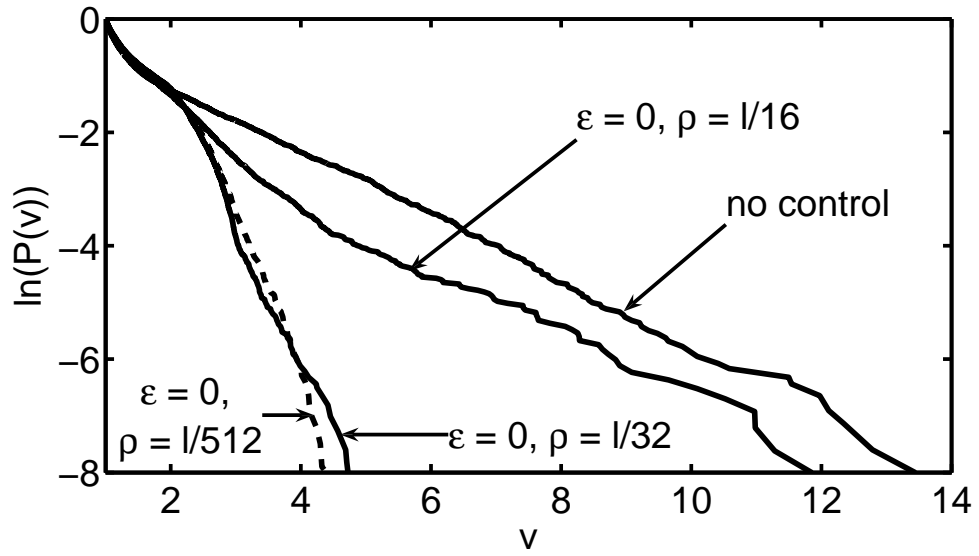


Figure 2.13: Comparison of $P(v)$ for the standard control parameters (2.12) for different observation densities, with $\rho = l/512, l/32, l/16$.

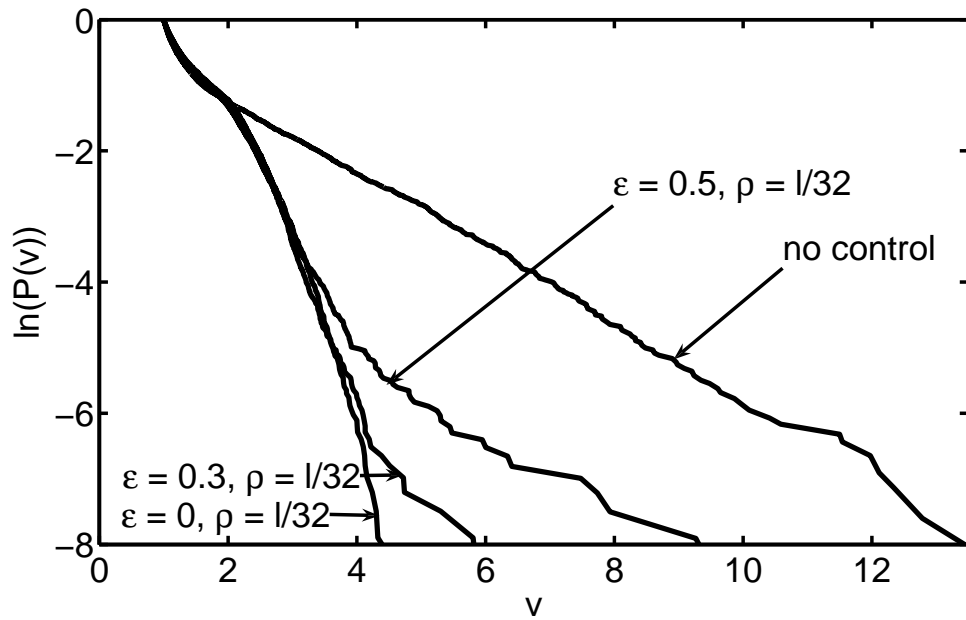


Figure 2.14: Comparison of $P(v)$ for the standard control parameters (2.12) for different noise levels ϵ with $\rho = l/512$ and $\rho = l/32$.

- A sufficiently accurate model of system dynamics.
- Access to measurements of the system state that are of sufficient accuracy and spatial and temporal resolution.
- The ability to physically make local control perturbations to the system.

Given that these prerequisites are satisfied, our numerical experiments suggest that it may, in some cases, be feasible to effectively control physical systems exhibiting rare intense events at low expense. In particular, we have shown how the information obtained from a forecast can be applied to formulate and implement spatially and temporally localized control. This is to be contrasted with previous work where spatiotemporal chaos was controlled either globally [4, 6, 35] or locally with controllers located at fixed spatial locations e.g, [36, 37]. Furthermore, while several studies, e.g, [4, 6, 35, 37], focused on forcing the controlled system to a non-chaotic region, e.g, towards plane wave solutions, our goal is not to significantly eliminate the chaotic nature of the dynamics, but rather to eliminate only its potentially most harmful part. This feature results in a potentially cost efficient control. We have found that time sequencing of control is a key issue for implementation of our control strategy, and we have investigated how control strength and cost are related to effectiveness. Moreover, model error and imperfect state measurement can impose important limitations.

We emphasize that our results may be limited in their applicability because of the simple ‘toy model’ we have employed (the CGL equation, Eq.(2.1)), and that many additional issues can arise when a program of this type is attempted for a real

physical system. We, nevertheless, hope that our results may provide some useful insight to real applications.

Chapter 3

Dynamics of a one dimensional self-organized model

3.1 Introduction

Over the last two decades, systems exhibiting self-organized behavior have attracted considerable attention. The term self-organized criticality (SOC), refers to extended dissipative systems that are driven into a critical, self-similar, and statistically stationary state independent of initial conditions, without the need to fine-tune the system parameters. Their common features can be characterized by slow driving energy input, with rare intense dissipation events, whose size distribution obeys a power law. Illustrating the versatility and applicability of SOC in nature, several examples have been identified. Sandpile models, which provide simple models for avalanches, have been investigated both numerically [38, 39] and analytically [40]. Additional examples are earthquake models [41], diffusion-limited aggregation [42], and invasion percolation models [43]. Many properties of SOC systems compare favorably to experimental data. For instance, good quantitative agreement was found between the interoccurrence time statistics of solar flares and the Bak-Tang-Wiesenfeld sandpile model [44].

Our focus is the self-organized forest-fire model (FFM), originally was introduced as a possible realization of SOC [45]. This model was later modified by introducing a lighting parameter to provide proper scaling behavior [46]. Computer

simulations [47, 46, 48] and analytical considerations [49] confirm that sufficient separation of time scales leads to SOC in the FFM. Mean field-theory approximations [50], an inverse-cascade model [51], and a renormalization group technique [52] were proposed as analytical approaches to understand the equilibrium of the FFM.

Previous work on the FFM has focused on understanding the statistically steady behavior. However, it is also of interest to examine situations where changes in the external conditions in these systems occur on a time-scale that is faster than, or of the order of the typical time needed for relaxation to the statistically steady state. As examples, we mention the following situations of interest.

- The forest system on a large island might be destroyed or otherwise globally effected by the occurrence of some major disaster such as a large volcanic eruption. In such a case one might be interested in the time evolution of the regrowing forest including the effect of forest fires. Thus one might be interested in the FFM dynamics starting from an initial condition far from the statistically steady state.
- The global conditions of a forest might be affected by climate changes. If these changes occur on a time scale shorter than, or of the same order as, the relaxation time to the FFM statistically stationary state, then consideration of dynamical processes away from the relaxed state is required.
- Normal seasonal weather changes can occur on a time scale that is comparable to the frequency of large snow avalanches.
- Self organized criticality also arises in scale-free networks [53] from local inter-

actions of large numbers of individuals. For instance, one might be interested in the dynamics of a computer network in the case of sudden introduction of a new technology or of sudden introduction of new connections and nodes to the system.

- One might be interested in reducing the number of rare and particularly destructive large forest fires by controlling the system dynamics, e.g., by preventing the formation of large connected patches of forest through controlled burns. In such a case, intermittent application of controls can place the state away from the statistical equilibrium towards which it subsequently begins to relax. This is a problem we intend to address in the future.

Here we investigate the *dynamical* behavior of the self-organized forest-fire model in one dimension, in the simplest case when burning of trees occurs instantaneously. The one-dimensional FFM is defined on a linear grid of L sites, which for simplicity is taken to be periodic. Each site can be in either of two states: empty (no tree on the site) or occupied (there is a tree on the site). The state of the system is updated in discrete steps using the positive real parameters $p \ll 1, f \ll 1$. In each step a tree is placed on the empty sites with probability p . If a site is occupied, then we ‘hit it with a lightning bolt’ with probability f which makes it ‘burn down’ turning it into an empty site. If we denote the time needed to burn down the largest clusters by T_{\max} (a cluster is a group of contiguous trees), then critical behavior in the FFM arises in the presence of double time scale separation, $T_{\max} \ll p^{-1} \ll f^{-1}$ [56]. The condition $T_{\max} \ll p^{-1}$ is most easily realized when fire spreads instantaneously to

every site that is part of the cluster containing a burning tree, which is the situation that we consider in the rest of this Chapter. A key parameter of the model is the ratio

$$\gamma = f/p, \tag{3.1}$$

which is assumed to be much less than one. Because the FFM is self-organized, it can be expected that any substantial departure from its equilibrium state will be followed by a relaxation process. Our goal is to understand how the dynamical behavior of the self organized forest fire model can be understood. As we shall see later, the time scale for relaxation to the statistically steady state is of the order of $1/p$ time-steps. Thus our object is to study the FFM dynamical process on the $1/p$ timestep scale. A hierarchy of steady-state equations for correlation functions of the FFM was proposed in [54]; and solved, as an approximation, with a mean-field closure scheme. An inverse cascade model was examined in [51], which reproduces several characteristics of the FFM. Here, we develop a hierarchy of equations that describes the dynamics of the FFM and can be closed to produce a set of self-consistent equations at any arbitrary level, thus producing a sequence of successively more accurate approximate descriptions of the dynamics. We use these equations along with numerical simulations to examine the relaxation properties of the FFM and the effect of non-steady external parameters of the model.

In Sec. II we present a discussion of the dynamics and examine an analytical approach for describing the non-equilibrium behavior of the one-dimensional FFM. In Sec. III we compare our analytical results with numerical simulations and discuss

the their validity. Finally, in Sec. IV we summarize our results and give conclusions.

3.2 Dynamics of the forest-fire model in one dimension

3.2.1 Framework

The one-dimensional model we consider is defined on a grid consisting of L sites with periodic boundary conditions. We now define what we mean by a ‘cluster’. In Fig. 3.1 each box represents a site. There are $L = 32$ sites shown, arranged on a circle, where the circular topology corresponds to the periodic boundary conditions of our model. An example of state is shown, where a symbol T labels a site occupied by a tree, and a symbol E labels an empty site. A cluster is a sequence of sites that are bounded by exactly one empty site on each side, and that has no empty sites in its interior. If there are two consecutive empty sites, we say that there is a cluster of size zero between them. Otherwise, the size of a cluster is defined as the number of trees between its bounding empty sites. For every $x \leq L$ we define

$$S_x = \# \text{ of clusters of size } x. \quad (3.2)$$

For example in Fig. 3.1 cluster sizes are indicated by the numbers shown outside the circle of sites, and $S_5 = 1, S_4 = 1, S_2 = 4, S_1 = 1, S_0 = 7$. In general, since each empty site bounds two clusters (one on each side), and each cluster bounds two empty sites, the number of empty sites, denoted N_e , equals the number of clusters,

$$N_e = \sum_{x=0}^L S_x, \quad (3.3)$$

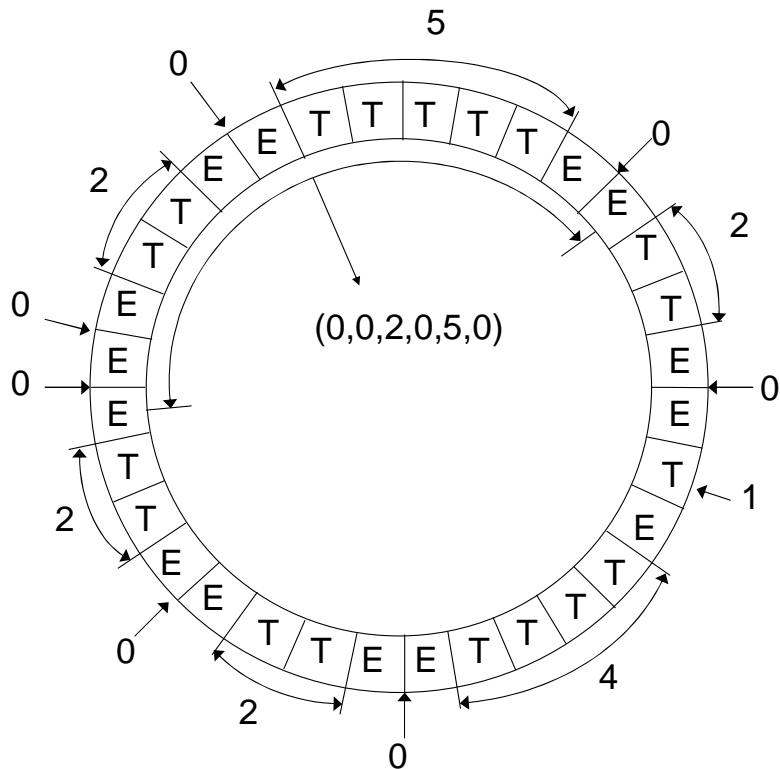


Figure 3.1: A state of the FFM for $L = 32$.

and the total number of sites can be expressed as

$$L = N_e + \sum_{x=0}^{\infty} x S_x. \quad (3.4)$$

As shown in Ref. [49] the statistically stationary S_x follows a simple power law distribution $S_x \sim x^{-2}$ for $\gamma x \ll 1$. As discussed in Sec. III A, statistical fluctuations of S_x in time are always present in the FFM, but become smaller as L increases.

We define an ‘ n -cluster configuration’ as a string of n clusters that occur consecutively (say in the clockwise direction in Fig. 3.1). We can describe such a configuration by giving the sizes of consecutive clusters using the notation (x_1, x_2, \dots, x_n) . For instance, corresponding to the six clusters bracketed by the arrowheads drawn inside the circle of sites in Fig. 3.1, we have the 6-cluster configuration $(0, 0, 2, 0, 5, 0)$.

Given a n -cluster (x_1, \dots, x_n) and a fixed value of $i = 1, \dots, n - 1$ we define $P_n(x_1, \dots, x_n)$ for $n \geq 2$ as the probability that a randomly chosen empty site is the one separating the clusters x_i and x_{i+1} in the configuration (note that this probability is the same for any choice of $i = 1, \dots, n - 1$). For the special case $n = 1$, we define $P_1(x)$ to be the probability that a randomly chosen empty site has a cluster of size x on its clockwise side, which is the same as the probability that it has a cluster of size x on its counterclockwise side. $P_1(x)$ is given by the number of clusters of size x divided by the number of empty sites, i.e.,

$$P_1(x) = S_x/N_e. \quad (3.5)$$

$P_2(x, y)$ is the probability that a randomly chosen empty site separates the clusters of the 2-cluster configuration (x, y) . For example, for the state shown in Fig. 3.1, we have $P_1(5) = 1/14$ and $P_2(0, 2) = 4/14$. The probability distribution for an $n - 1$ cluster configuration, P_{n-1} , can be calculated as the marginal probability of P_n ,

$$\sum_{x_n=0}^L P_n(x_1, \dots, x_n) = P_{n-1}(x_1, \dots, x_{n-1}). \quad (3.6)$$

In particular for $n = 2$ we have

$$\sum_{y=0}^L P_2(x, y) = P_1(x) = S_x/N_e. \quad (3.7)$$

Assuming statistical isotropy for $L \gg 1$, we postulate that $P_n(x_1, \dots, x_n)$ is invariant to reflections of the grid, which implies that $P_n(x_1, \dots, x_n) = P_n(x_n, \dots, x_1)$.

3.2.2 Continuous time approximation

Our goal is to understand how P_n evolves in time in situations far from the stationary state. We start with the following observations. When placing a tree on an empty site between a cluster of size x and a cluster of size y (i.e., a 2-cluster configuration (x, y)), a new cluster of size $x + y + 1$ is created by coalescing the two neighbors. In the special case when an empty site is surrounded by empty sites on both sides (i.e., $x = 0, y = 0$), addition of a tree will create a cluster of size one.

There are two possible ways for a cluster to change its size. It can either burn down or a tree can be added at its boundary. The probability that a cluster of size x burns down in one step is $1 - (1 - f)^x$. We assume in what follows that $xf \ll 1$ so that

$$1 - (1 - f)^x \simeq xf. \tag{3.8}$$

Addition of a tree at one of the two empty sites on the cluster's boundary occurs with probability

$$1 - (1 - p)^2 \simeq 2p, \tag{3.9}$$

where we assume $p \ll 1$. Since p and xf are small, the probability that both of these events happen simultaneously (i.e., a tree is added to a cluster which burns down) is negligible compared to p and xf . Similarly, the probability that we add two trees to the same cluster is of order p^2 and also can be neglected. According to Eqs. (3.8) and (3.9) the expected number of clusters of size x that either become

larger or burn down in one step is

$$S_x(x\gamma + 2)p \text{ (for } p \ll 1, \gamma = f/p). \quad (3.10)$$

On the other hand, S_x can grow if two neighboring clusters of sizes x_1, x_2 with $x = x_1 + x_2 + 1$ coalesce, by addition of a tree to the empty site that separates them.

The expected number of such empty sites is $N_e \sum_{a+b+1=x} P_2(a, b)$, which combined with (3.10) gives the dynamical equation,

$$S_{x,m+1} - S_{x,m} = p_m N_{e,m} \sum_{a+b+1=x} P_2(a, b; m) - p_m(2 + \gamma_m x) S_{x,m}.$$

where $x > 0$ and m denotes the model time step with $S_{x,m}$, $N_{e,m}$, and $P_2(a, b; m)$ the value of S_x , $P_2(a, b)$, and N_e at timestep m , and we now allow for time variation of p and γ via the replacements $p \rightarrow p_m$, $\gamma \rightarrow \gamma_m$. We approximate (3.11) for $p_m \ll 1$ by a continuous time description using a scaled time variable,

$$t = \sum_{k=1}^m p_k, \quad (3.11)$$

and introducing the following notations, $S_{x,m} = S_x(t)$, $N_{e,m} = N_e(t)$, $p_m = p(t)$,

$\gamma_m = \gamma(t)$, $P_n(x_1, \dots, x_n; m) = P_n(x_1, \dots, x_n; t)$, $dS_x(t)/dt = (S_{x,m+1} - S_{x,m})/p$.

Thus (3.11) (which applies for $x > 0$) becomes

$$\frac{dS_x(t)}{dt} = N_e(t) \sum_{a+b+1=x} P_2(a, b; t) - [2 + \gamma(t)x] S_x(t). \quad (3.12)$$

$S_0(t)$ grows because clusters burn down and becomes smaller because empty sites become occupied,

$$\frac{dS_0(t)}{dt} = -2S_0(t) + \gamma(t) \sum_{y=1}^L y(y+1) S_y(t). \quad (3.13)$$

Summing $S_x(t)$ for all x 's according to (3.3) gives

$$\frac{dN_e(t)}{dt} = -N_e(t) + \gamma(t) \sum_y y^2 S_y(t). \quad (3.14)$$

As a check, we note that Eqs. (3.12) and (4.38) are consistent with the requirement of site conservation, which using (3.4) can be expressed as

$$\frac{d}{dt}(N_e(t) + \sum_y y S_y(t)) = 0. \quad (3.15)$$

Using $P_1(x; t) = S_x(t)/N_e(t)$, Eq. (3.12) can be rewritten in terms of probabilities,

$$\frac{d(N_e(t)P_1(x; t))}{dt} = N_e(t) \sum_{a+b+1=x} P_2(a, b; t) - [2 + \gamma(t)x] N_e(t)P_1(x; t),$$

which is the first step in a hierarchy of equations for P_n 's, to be discussed in the following subsection. Equations (3.12) and (4.38) describe the evolution of $S_x(t)$ if $P_2(a, b; t)$ is known. As we intend to give a general description of the model, we cannot assume $P_2(a, b; t)$ to be in its equilibrium form. In what follows we explain how a sequence of approximations can be obtained, with each step providing a more accurate description of the model.

3.2.3 Estimation of $P_2(a, b; t)$

As a motivating example, we first consider the case where we start $t = 0$ with a completely empty grid, i.e., $N_e(0) = S_0(0) = L$ and $S_x(0) = 0$ for all $x > 0$. We begin by assuming that the time elapsed since the start of the experiment is short enough that large clusters have not yet formed and that burning does not have a significant impact, i.e., $x\gamma \ll 1$. If the effect of fire is negligible, then the probabilities that any two sites are occupied are uncorrelated, and thus the probabilities of an

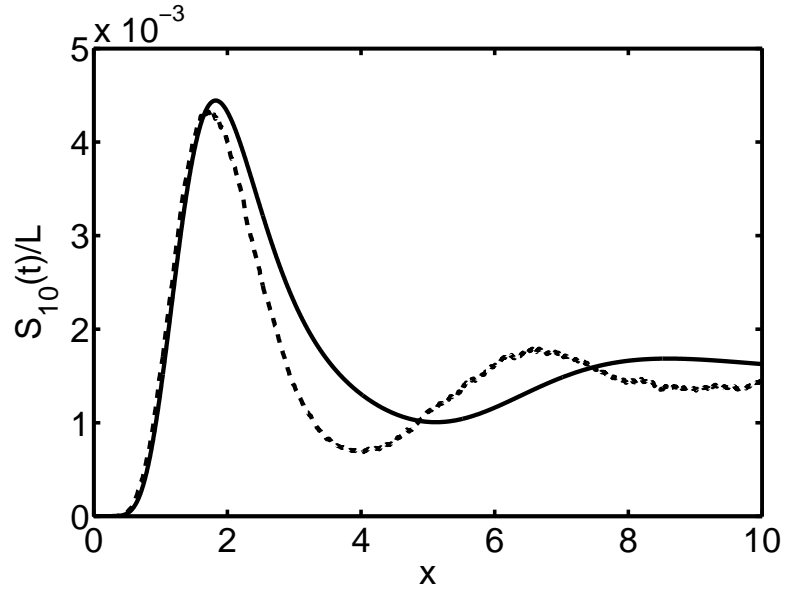


Figure 3.2: S_{10}/L versus time t for $\gamma = 5 \times 10^{-3}$ and $L = 10^6$ with empty grid initial conditions. The dash-dotted curve is the result from a full numerical simulation, while the solid curve is from the solution of (3.14) and (3.17).

empty site having a cluster of size x on its left and a cluster of size y on its right are independent. Hence

$$P_2(x, y; t) = P_1(x; t)P_1(y; t). \quad (3.16)$$

If we assume Eq. (3.16) to hold, then Eq. (3.12) takes the form,

$$\frac{dS_x(t)}{dt} = \frac{1}{N_e(t)} \sum_{a+b+1=x} S_a(t)S_b(t) - [2 + \gamma(t)x] S_x(t). \quad (3.17)$$

The time dependent solution of (3.17) for $L \gg 1$ and $\gamma \sum_y y^2 S(y, t) \ll 1$ can be expressed explicitly as a function of $N_e(t)$ using a generating function technique as shown in the Appendix. Equation (3.17) combined with (3.14) determines the dynamics when $P_2(a, b; t)$ is approximately in the form (3.16). Eventually, clusters will grow so large that the assumed conditions under which (3.17) is valid will no longer be satisfied. To understand why this happens consider the situation when

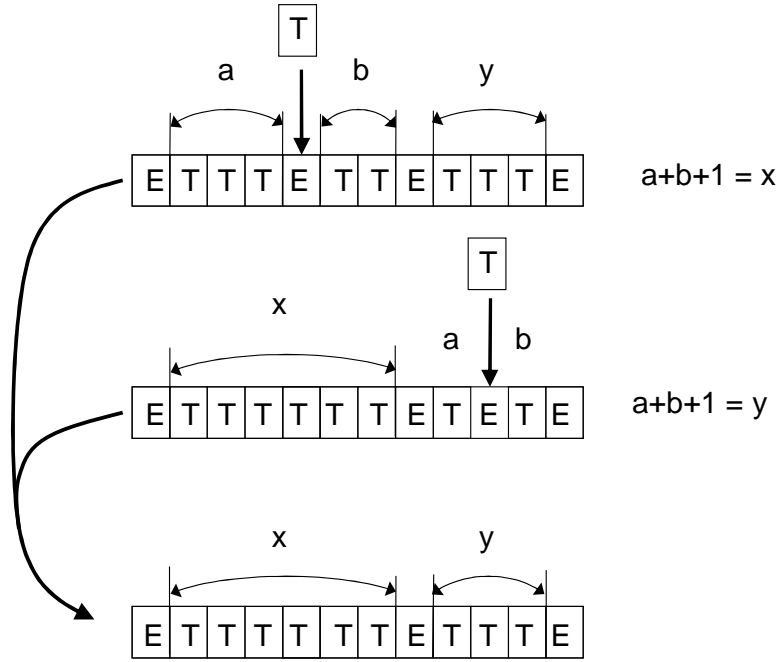


Figure 3.3: 2-clusters are created by coalescing 3-cluster configurations.

a large forest cluster burns down. This creates a long string of adjacent empty sites, that will change the uniform distribution created by the slow driving input of tree growth, and (3.16) will no longer hold. At large time this effect will be more pronounced as we decrease the value of γ , since lowering γ leads to larger time-asymptotic correlation length $\xi_c \sim \gamma^{-\nu}$, see Ref. [55]. Figure 3.2 shows S_{10} versus time with $\gamma = 5 \times 10^{-3}$ and $L = 10^6$ from a full numerical simulation of the FFM system (dotted curve) and from the solution of the approximating system Eq. (3.17) and (3.14) (solid curve). From such plots we find that the accuracy of (3.17) is relatively good for $\gamma = 5 \times 10^{-3}$, if $t < 2.5$. We will examine this in more detail in Sec. III.

We now turn to describe the dynamics of $P_2(x, y; t)$. The number of empty sites on the grid that separates the x and y clusters of the 2-cluster (x, y) is $N_e(t)P(x, y; t)$.

A 2-cluster (x, y) can be created in one step by adding a tree to appropriate 3-clusters: As shown in Fig. 3.3, the two cluster (x, y) will be created from (a, b, y) or (x, a, b) if a tree is grown in the empty site separating the a and b clusters and if $a + b + 1 = x$ in the first case or if $a + b + 1 = y$ in the second case. According to its definition $P_3(u, v, w; t)$ is the probability that a randomly chosen empty site is the one separating the u and v clusters (which is the same as the probability that it separates the v and w clusters) in the 3-cluster (u, v, w) . Accordingly, the expected number of configurations of type (x, y) created by tree growth in one step is

$$\sum_{a+b+1=y} p(t)N_e(t)P_3(x, a, b; t) + \sum_{a+b+1=x} p(t)N_e(t)P_3(a, b, y; t) \quad (3.18)$$

On the other hand, the number of 2-cluster configurations (x, y) decreases if either a tree is added to any of the three empty sites bounding x and/or y (these three empty sites are: the one to the left of x -cluster, the one between the x and y clusters, and the one to the right of the y -cluster). As a result, the expected number of 2-clusters of type (x, y) destroyed because of addition of trees is $3p(t)N_e(t)P_2(x, y; t)$. Finally, fires can destroy either x or y in a configuration (x, y) which decreases the number of (x, y) 2-clusters by $p(t)\gamma(t)N_e(t)P_2(x, y; t)(x + y)$. Summarizing, we have

$$\begin{aligned} \frac{d(N_e(t)P_2(x, y; t))}{dt} = & - [3 + \gamma(t)(x + y)] N_e(t)P_2(x, y; t) + \\ & + \sum_{a+b+1=x} N_e(t)P_3(a, b, y; t) + \sum_{a+b+1=y} N_e(t)P_3(x, a, b; t), \end{aligned} \quad (3.19)$$

for $(x > 0, y > 0)$. Thus the solution of P_2 depends on P_3 (similar to the dependence of the evolution of P_1 on P_2 in Eq. (3.18)). We have to consider the case when either $x = 0$ or $y = 0$ separately, because clusters of type $(0, x)$ will have positive

contribution from all clusters of type (a, x) , $a > 0$ if a , burns down. If $x = 0$ and $y > 0$ then we have to add $\sum_a N_e(t)P_2(a, x; t)a\gamma(t)$ to the right side of (3.19) which yields,

$$\begin{aligned} \frac{d(N_e(t)P_2(0, y; t))}{dt} = & -[3 + \gamma(t)y] N_e(t)P_2(0, y; t)+ \\ & + \sum_{a+b+1=y} N_e(t)P_3(0, a, b; t) + \sum_a N_e(t)P_2(a, y; t)a\gamma(t). \end{aligned} \quad (3.20)$$

The equation for $N_e(t)P_2(0, 0; t)$ can be obtained if we combine (3.19) and (3.20) with the normalizing condition $\sum_{x,y} P_2(x, y; t) = 1$. It can be shown that Eqs. (3.19) and (3.20) are consistent with our previous dynamical equation Eq. (3.12) using (3.6).

We can similarly continue this sequence of equations, e.g., the dynamics of $N_e P_n$ for $x_i > 0$, ($i = 1, 2, \dots, n$) is given by,

$$\begin{aligned} \frac{d(N_e(t)P_n(x_1, \dots, x_n))}{dt} = & - \left[n + 1 + \gamma(t) \left(\sum_{i=1}^n x_i \right) \right] N_e(t)P_n(x_1, \dots, x_n; t)+ \\ & + N_e(t) \sum_{j=1}^n \sum_{a+b=x_j} P_{n+1}(x_1, \dots, x_{j-1}, a, b, x_{j+1}, \dots, x_n; t), \end{aligned} \quad (3.21)$$

where in the sum over j we define the first and last terms of the sum ($j = 1$ and $j = n$) so that the argument of P_{n+1} is (a, b, x_2, \dots, x_n) for $j = 1$ and $(x_1, \dots, x_{n-1}, a, b)$ for $j = n$. Thus we obtain a sequence of descriptions in which the evolution of $P_n(x_1, x_2, \dots, x_n; t)$ depends on the higher order probability functions $P_{n+1}(x_1, x_2, \dots, x_{n+1}; t)$. We can truncate the resulting equation for a given $P_n(x_1, x_2, \dots, x_n; t)$ by making the assumption that for an $(n + 1)$ -cluster configuration of type (x_1, \dots, x_{n+1}) the probability distribution of x_1 does not depend on

x_{n+1} which can be stated in terms of conditional probabilities,

$$\tilde{P}_{n+1}(x_1|x_2, \dots, x_{n+1}; t) \cong \tilde{P}_n(x_1|x_2, \dots, x_n; t). \quad (3.22)$$

This supposition is equivalent to assuming a limited correlation length and is supported by the numerical observation that, in the statistically steady state, the correlation function decays exponentially with the distance [55]. Relationship (3.22) along with Bayes' theorem can be used to obtain

$$\begin{aligned} P_{n+1}(x_1, \dots, x_{n+1}; t) &= \tilde{P}_{n+1}(x_1|x_2, \dots, x_{n+1}; t)P_n(x_2, \dots, x_{n+1}; t) \approx \\ &\approx \tilde{P}_n(x_1|x_2, \dots, x_n; t)P_n(x_2, \dots, x_{n+1}; t), \end{aligned} \quad (3.23)$$

where we have used (3.22) to approximate \tilde{P}_{n+1} by \tilde{P}_n . Now again using Bayes' theorem we have $\tilde{P}_n(x_1|x_2, \dots, x_n; t)P_{n-1}(x_2, \dots, x_n) = P_n(x_1, \dots, x_n; t)$, which we use to eliminate \tilde{P}_n in (3.23), resulting in

$$\frac{P_n(x_1, \dots, x_n; t)P_n(x_2, \dots, x_{n+1}; t)}{P_{n-1}(x_2, \dots, x_n; t)}, \quad (3.24)$$

and P_{n-1} can be expressed in terms of P_n by use of Eq. (3.6), $P_{n-1}(x_2, \dots, x_n; t) = \sum_{x_1} P_n(x_1, \dots, x_n; t)$. The importance of (3.24) is that it expresses P_{n+1} as a function of lower-order probabilities P_n and P_{n-1} , which combined with the dynamical equations, e.g., (3.21), gives a closed set of first-order ordinary differential equations. The highest-order approximation we will examine in the following section is given by Eqs. (3.19) and (3.20). In this case we close our hierarchy of equations with

$$P_3(a, b, c; t) = \frac{P_2(a, b; t)P_2(b, c; t)}{P_1(b; t)}. \quad (3.25)$$

3.3 Numerical experiments

3.3.1 Relaxation time

We introduce a measure characterizing the difference between two cluster size distributions, S_x and S_x^* ,

$$\Delta(S_x, S_x^*) = \left(|N_e - N_e^*| + \sum_{x=0}^L |S_x - S_x^*| x \right) / (2L). \quad (3.26)$$

By (3.4) we have that $0 \leq \Delta \leq 1$. As an indication of how the system relaxes to its time asymptotic steady state when γ is time-independent, Fig. 3.4 shows plots of $\Delta(S_x(t), S_x(\infty))$ versus t , where $S_x(t)$ is calculated from the FFM with different initial conditions, and $S_x(\infty)$ is calculated as an average over a long time interval $[t_1, t_2]$ where t_1 is large. In particular, as initial conditions for calculating $S_x(t)$ we took the steady-state solution $S_x(\infty)$ of the FFM and eliminated clusters that were larger than a chosen cutoff value x_{\max} . I.e., if an occupied site belongs to a cluster of size $x \geq x_{\max}$, we replace that occupied site by an empty site.

We see from Fig. 3.4 that for a fixed γ , a broad range of perturbations agree in the order of magnitude in their relaxation timescales as measured by Δ . Because Δ involves an average over all x , we refer to the relaxation of Δ as a ‘global relaxation’. Later (in subsection C) we will examine the relaxation of S_x as a function of x , and will find x -dependent ‘local’ time-scales. Again referring to Fig. 3.4, we note that, because of statistical fluctuations, none of the curves converge to exactly zero. For the chosen γ and system size of $L = 10^6$ used in Fig. 3.4, the statistical fluctuation between the time-asymptotic $S_x(t)$ and $S_x(\infty)$ is around $\Delta \approx 8 \times 10^{-2}$. As a

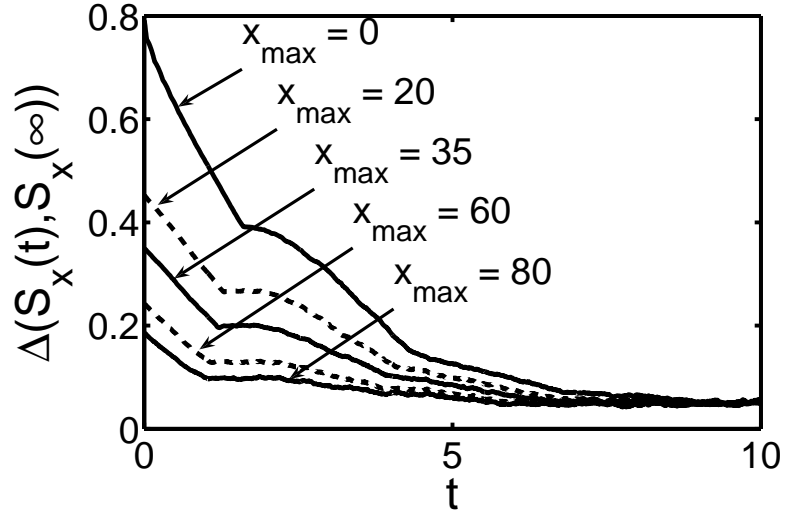


Figure 3.4: Difference between the perturbed and time-asymptotic distributions for different initial conditions with $\gamma = 5 \times 10^{-3}$ and $L = 10^6$.

comparison, $L = 10^5$ results in $\Delta = 0.13$ and $L = 10^7$ leads to $\Delta = 2.2 \times 10^{-2}$.

According to our observations, for a fixed gridsize L , the lower γ , the higher the level of statistical fluctuations. In particular, if γ is too small, e.g., $\gamma < 10^{-4}$ for $L = 10^6$, the effect of fluctuations of $S_x(t)$ becomes so large that it is comparable in magnitude to $S_x(t)$ itself.

3.3.2 Accuracy of our approximate descriptions of FFM dynamics

To assess the accuracy of our analytical considerations, we now compare the dynamics predicted by (3.19)-(3.20), and (3.17) with time-independent γ to full numerical simulations of the FFM. For the solution of the full FFM we used a gridsize $L = 10^6$, with $p = 5 \times 10^{-4}$ and $f = p\gamma$, with $\gamma = 5 \times 10^{-2}, 10^{-2}, 5 \times 10^{-3}, 2 \times 10^{-3}, 5 \times 10^{-5}$. For the numerical solution of (3.19) and (3.20) we proceed as follows. Equations (3.19) and (3.20) determine the time evolution of the probability function

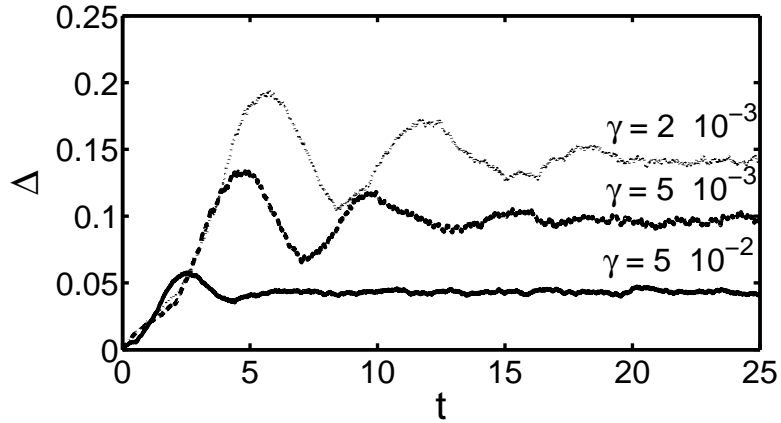


Figure 3.5: The accuracy parameter Δ versus time with $L = 10^6$ and $\gamma = 5 \times 10^{-2}, 5 \times 10^{-3}, 2 \times 10^{-3}$ for the second-order approximation (3.19) and (3.20).

$P_2(x, y; t)$, which at each time t depends on the variables x and y . Thus we have to solve the equations on a two-dimensional grid of size $L \times L$. However, it is known from the statistically steady solution of the full FFM [46], that for a given γ there exists a size limit above which forest clusters are extremely rare. Therefore, instead of solving (3.19) and (3.20) for all clusters sizes, between 0 and $L = 10^6$, we restrict our attention to the most frequently occurring ones and solve the Eqs. (3.19) and (3.20) on a two dimensional grid (x, y) of size 500×500 .

Equation (3.12) is the first in our hierarchy of equations and therefore from now on we will refer to it as the first-order approximation. Similarly, the dynamics determined by Eqs. (3.19) and (3.20) will be called the second-order approximation. Figure 3.5 shows $\Delta(S_x(t), S_x^*(t))$ versus t for three different values of γ versus t , where $S_x(t)$ is obtained from the second-order approximation and $S_x^*(t)$ is the result from numerical solution of the FFM. For both, the initial condition was an empty grid (i.e., $N_e(0) = S_0(0) = L$ and $S_x(0) = 0$ for $x \geq 1$). It is seen that, if $\Delta(t)$ at large time (denoted Δ_∞) is larger for one value of γ than for another, then this is generally

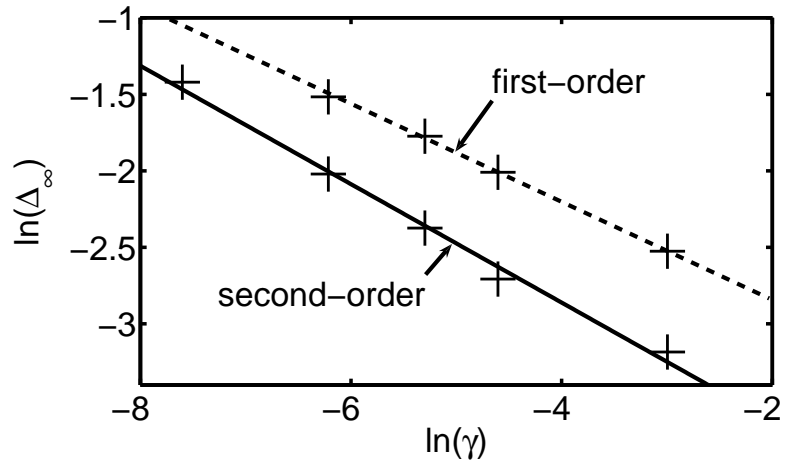


Figure 3.6: The accuracy parameter Δ_∞ versus the forest-fire intensity γ , for the second-order model given by (3.19) and (3.20) (solid curve) and for the first-order model given by (3.17) (dashed curve). $L = 10^6$.

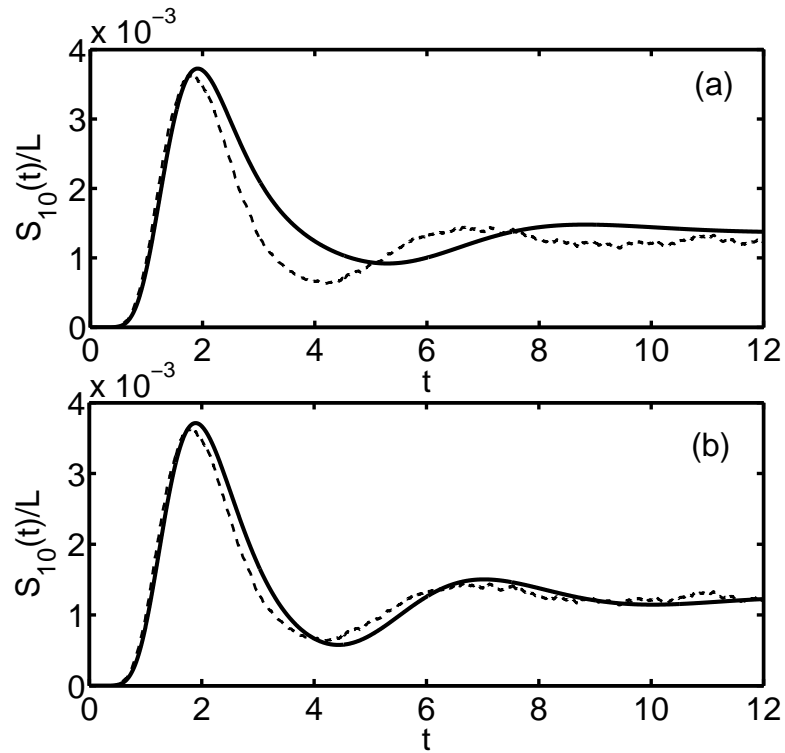


Figure 3.7: S_{10} versus time t for $\gamma = 5 \times 10^{-3}$ and $L = 10^6$ with empty grid initial conditions. The dotted curves are the results from a full numerical simulation of the FFM, while the solid curves in (a) and (b) correspond respectively to the first and second-order approximation.

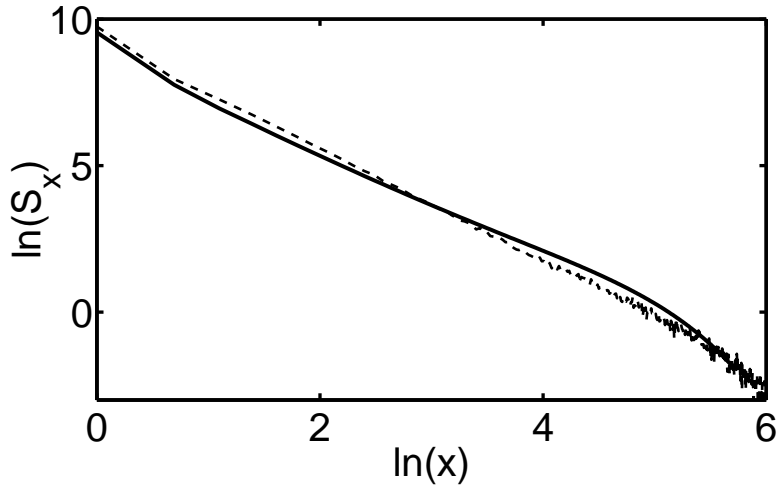


Figure 3.8: The time-asymptotic $\ln(S_x)$ versus $\ln(x)$. The dotted curve is the result from a full numerical simulation of the FFM, while the solid curve is from the second-order approximation. The parameter values are $\gamma = 5 \times 10^{-3}$, $L = 10^6$.

also true for Δ at other times. Thus we characterize the overall accuracy by Δ_∞ . Figure 3.6 shows Δ_∞ versus γ for the first and second order approximations. We note that statistical fluctuations account for some of the difference between the S_x and S_x^* . It is apparent that the second-order approximation performs significantly better than the first-order approximation. Our results also indicate that decreasing γ increases Δ_∞ . The log-log plot shown in Fig. 3.6 demonstrates that Δ_∞ versus γ is consistent with a power law dependence,

$$\Delta_\infty \sim \gamma^{-a}. \quad (3.27)$$

for both the second-order approximation, $a \simeq 0.38$, and the first-order approximation, $a \simeq 0.31$. Figure 3.7 compares the time dependence of $S_{10}(t)$ from the full FFM with the time dependence obtained from the first-order approximation (solid curve in Fig. 3.7 (a)) and from the second-order approximation (solid curve in Fig. 3.7 (b)). The second-order method predicts the time dependence of the evolution

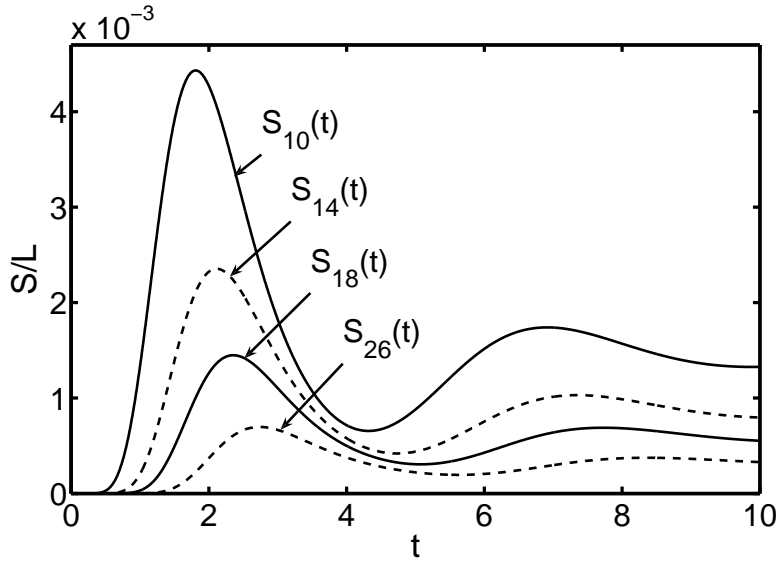


Figure 3.9: S_x versus time t for $\gamma = 5 \times 10^{-3}$, $L = 10^6$, and $x = 10, 14, 18, 26$ for the second-order approximation with empty grid initial conditions.

(Fig. 3.7 (b)) and the time-asymptotic form of S_x very well. Figure 3.8 shows the time asymptotic cluster size distribution $S_x(\infty)$ versus x obtained from solution of our second-order equations (solid curve) and from a numerical calculation of the full FFM (dots). Again we see very good agreement.

3.3.3 Cluster-size dependent dynamics

We now examine how the relaxation dynamics of $S_x(t)$ for time-independent γ depends on the cluster size x . Figure 3.9 shows $S_x(t)$ from the second-order approximation with empty grid initial conditions for cluster sizes $x = 10, 14, 18, 24$. When the FFM evolves, starting with a completely empty grid as initial condition, the first maximum that $S_x(t)$ reaches will also be its global maximum in time, as shown in Fig. 3.7. From Fig. 3.9 it is apparent that larger clusters reach this maximum later in time. This can be interpreted as being due to the extra time

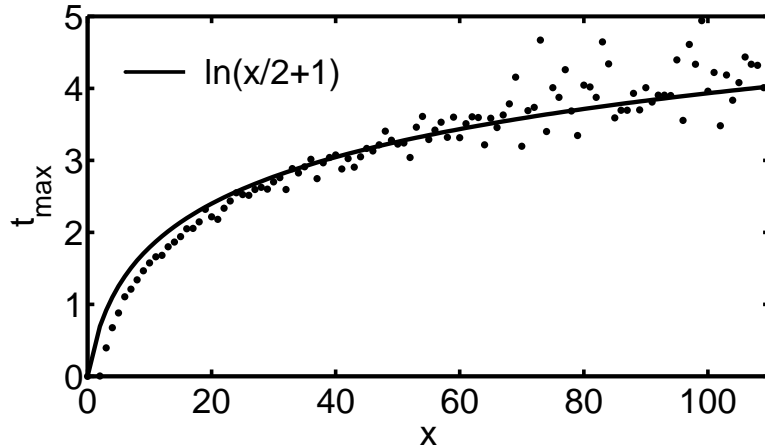


Figure 3.10: $t_{max}(x)$ versus x for $\gamma = 5 \times 10^{-3}$, $L = 10^6$. The dots are the results from a full numerical simulation of the FFM, while the solid curve is the analytical result from the first-order approximation, i.e., $t_{max}(x) = \ln(x/2 + 1)$ (Eq. (4.47)).

taken by the coalescence process that creates larger clusters from smaller ones. In the absence of forest fires, i.e., $\gamma = 0$, $S_x(t)$ would relax to $S_x(t) = 0$ for $x < L$, after this maximum is reached, as seen from the analytical solution presented in the Appendix. In the presence of forest fires, however, $S_x(t)$ oscillates around its time asymptotic value until complete relaxation is achieved.

We examine the accuracy of the first-order approximation's ability to predict the time of the first maximum of $S_x(t)$. For every cluster size x we define $t_{max}(x)$ to be the time instant when S_x reaches its first maximum value. An approximate analytical expression $t_{max} \approx \ln(x/2 + 1)$ is obtained in Appendix A. Thus the characteristic time scale for evolution of S_x as characterized by t_{max} is predicted to be longer for larger x (i.e., larger cluster sizes). Figure 3.10 compares the calculated and the analytical $t_{max}(x)$ data for $\gamma = 5 \times 10^{-3}$. We see that the full FFM simulation results for t_{max} are in good agreement with our first-order approximation.

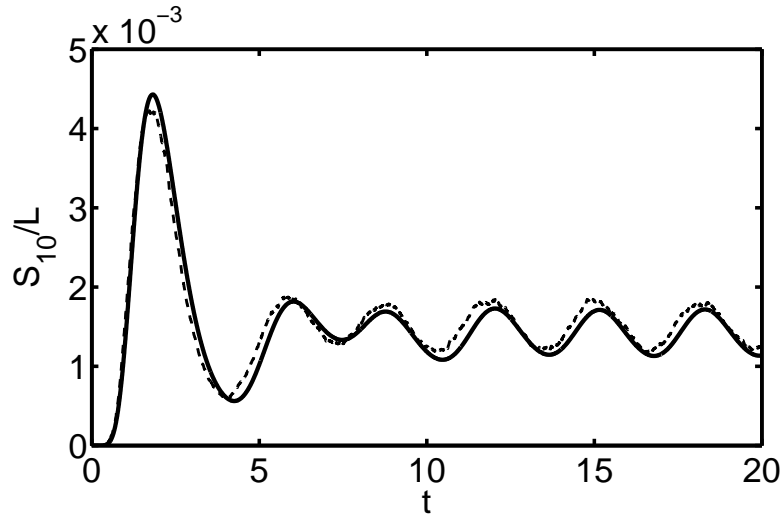


Figure 3.11: S_{10}/L versus t for $\gamma_0 = 5 \times 10^{-3}$, $L = 10^6$, $\omega = 1$, and $A = 0.5$. The dotted curve is the result from the FFM, while the solid curve is from the second-order approximation.

3.3.4 Dynamics for time dependent $\gamma(t)$

As a final experiment we examine the ability of our second-order approximation to describe the behavior of the FFM when $\gamma(t)$ depends on time. For our experiment we chose

$$\gamma(t) = \gamma_0 (1 + A \sin(\omega t)) \text{ with } A < 1, \quad (3.28)$$

with $\gamma_0 = 5 \times 10^{-3}$. We explore the dependence of our results on the driving amplitude A and frequency ω . Consistent with our expectation, we found that, after the transients related to initial conditions relax, $S_x(t)$ shows temporally periodic oscillatory behavior at the frequency ω , $S_x(t) = S_x(t + 2\pi/\omega)$, as shown in Fig. 3.11. $S_x(t)$ has an approximately sinusoidal time dependence for sufficiently small amplitudes and large frequencies, e.g., if $A = 0.5$, and $\omega = 1$, as shown in Fig. 3.11. With the increase of the driving amplitude and lowering of the frequency, this

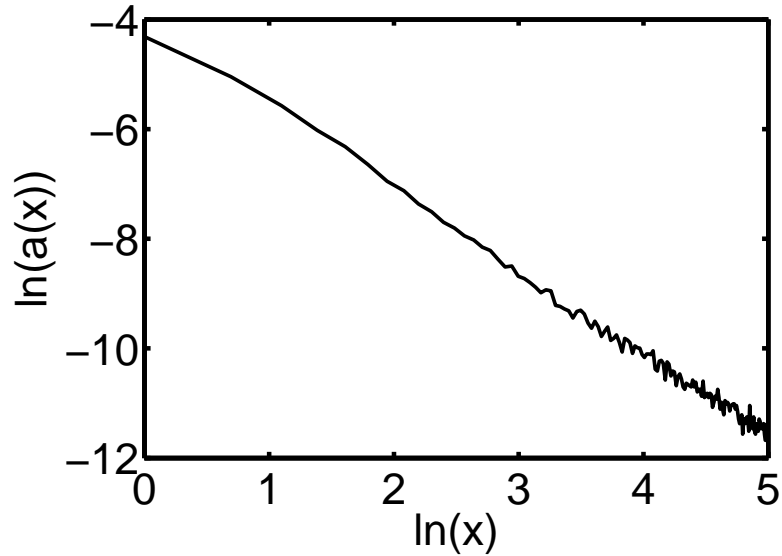


Figure 3.12: The amplitude of oscillation $a(x)$ versus the cluster size x for $\gamma_0 = 5 \times 10^{-3}$, $L = 10^6$, $\omega = 1$, and $A = 0.5$.

sinusoidal waveform is distorted. For cases where $S_x(t)$ is approximately sinusoidal, we find that the amplitude of the oscillation of S_x , denoted $a(x)$, has an approximate power law dependence on the cluster size x , i.e., $a(x) \sim x^{-\alpha}$, with an exponent $\alpha \simeq 1.56$ (see Fig. 3.12), and the midpoint of the oscillation is, to within our available accuracy, the same as for the equilibrium solution of the FFM with $\gamma(t)$ set to a steady value γ_0 . The dependence of $a(1)$ on the driving frequency ω is shown in Fig. 3.14. The maximum amplitude of $a(x)$ for each cluster size x is attained at the resonant frequency $\omega_0 \simeq 1.14$. In the limit $\omega \rightarrow 0$ the system adiabatically oscillates among steady state solutions corresponding to different constant γ values. I.e., if we denote the steady state solution corresponding to a fixed value of γ by $S_x(\infty, \gamma)$ then $S_x(t) \simeq S_x(\infty, \gamma(t))$ for $\omega \ll \omega_0$, which for $A = 0.5$ and $\gamma_0 = 5 \times 10^{-3}$ leads to a non-vanishing oscillation amplitude $a(1) = 2.5 \times 10^{-3}$.

The existence of the resonant frequency is due to the presence of a character-

istic time-scale in the steady state, denoted T , which is defined as the average time needed for an empty site to become occupied and empty again. In order to give an estimate for T , consider the following. The probability that an empty site becomes occupied after time t equals $1 - e^{-t}$, leading to an average time for tree growth 1. If N_e denotes the number of empty sites in the steady state, then the number of trees grown on the grid in one timestep is $N_e p$, which equals the number of trees destroyed. Therefore, the fraction of trees destroyed in one timestep is $pN_e/(L - N_e)$. Assuming a constant rate of destruction for all trees, the probability that a tree burns down after time t equals $1 - \exp(-tN_e/(L - N_e))$, leading to an average lifetime $(L - N_e)/N_e$. As a result, we have $T = 1 + (L - N_e)/N_e = 1/(N_e/L)$, which corresponds to the frequency $\omega = 2\pi N_e/L \approx 1.07$, using the measured result $N_e/L \simeq 0.17$ for $\gamma = 5 \times 10^{-3}$. Resonance occurs when we drive the system at a frequency corresponding the characteristic timescale.

We define a phase shift $\Delta\phi(x)$ by which the oscillation of $S_x(t)$ lags that of $\gamma(t)$. Figure 3.13 shows $\Delta\phi(x)$ versus the cluster size x , with the solid curve corresponding to the second-order approximation and the dots to the full FFM. Burning of large clusters simultaneously creates many zero size clusters, therefore zero size clusters oscillate close in phase to larger ones seen illustrated in Fig. 3.13 (note that $\Delta\phi = 0$ and $\Delta\phi = 2\pi$ are equivalent). Furthermore in the region of large burns, small size clusters begin to form through tree growth and coalesce in time to form larger clusters, leading to the decrease of $\Delta\phi$ with increasing x (seen in Fig. 3.13). Figure 3.15 shows $\Delta\phi$ as a function of clustersize x , obtained from the second-order approximation, for the frequencies $\omega = 1, 2, 4$. An important point is

that for $\omega > 1.5$ the phase difference $\Delta\phi(x)$ has a local minimum. Figure 3.16 shows S_{10} versus S_6 starting from empty grid initial conditions as obtained from the second order approximation (Fig.3.16 (a)) and from the full FFM (Fig.3.16 (b)). From both we see the effect of the difference between $\Delta\phi(10)$ and $\Delta\phi(6)$ as manifested by the elliptical shape of the trajectory $S_{10}(t)$ versus $S_6(t)$, and that the oscillation of $S_6(t)$ leads that of $S_{10}(t)$, $\Delta\phi(10) > \Delta\phi(6)$ consistent with Fig. 3.13.

3.4 Conclusion

We examined *dynamical* behavior of the self-organized forest-fire model in one dimension, on a time scale that is faster than, or of the order of the time needed for relaxation of the system to the statistically steady-state. We found that, similarly to the statistically steady state behavior, the parameter γ plays a crucial role in determining the dynamics. From a computational point of view, we found that for a given grid size L , decreasing γ increases the effect of statistical fluctuations, which makes the study of the dynamical behavior via solution of the full FFM less effective. This becomes even more pronounced for larger cluster sizes. As an alternative, we introduced an analytical approach, based on a hierarchy of equations, which correspond to the $L \rightarrow \infty$ limit of the FFM. The closure scheme for this hierarchy, which is equivalent to assuming a limited correlation length, gives a set of self-consistent, successively more accurate approximations to the dynamics. The agreement between our hierarchy of equations and the numerical solutions of the full FFM depends on the forest fire intensity γ . Since decrease of γ leads to larger

correlation length [55], in order to accurately treat smaller lighting intensities γ , one would have to go to higher order approximations in our hierarchy. We found very good agreement between our second-order approximation and numerical simulations of the FFM for $\gamma \geq 2 \times 10^{-3}$.

The relaxation of the FFM to its time-asymptotic value, measured by the distance between distributions (in the sense (3.26)), can be characterized by a single relaxation time scale over a range of initial conditions (for a fixed γ). Relaxation measured by (3.26) characterizes the process in a global sense. On the other hand, locally for each individual cluster size, a cluster-size-dependent time-scale exists. We examined this effect, starting from empty grid initial conditions, and found that the time at the occurrence of the first maximum of $S_x(t)$, has an approximate logarithmic dependence on the cluster size. This is due to the fact that larger clusters are created through a cascading process from smaller ones, leading to a time delay.

To examine the effect of temporally changing external conditions on the FFM, we investigated the effect of a time-dependent forest fire intensity $\gamma(t)$. We found that for a sinusoidal $\gamma(t)$, that (i) the numbers of clusters of size x , $S_x(t)$, oscillates at the same frequency as $\gamma(t)$; (ii) the amplitude of the oscillation is a power-law function of the cluster size; and (iii) there is a cluster-size-dependent phase lag.

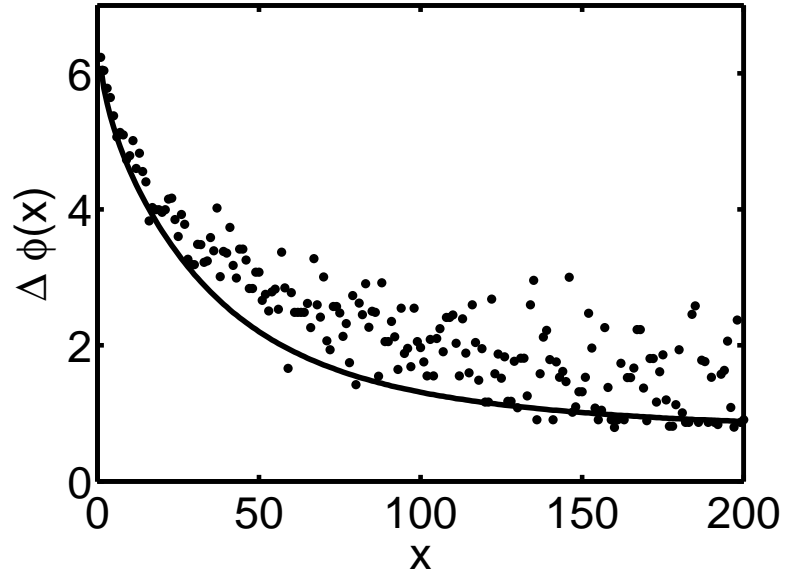


Figure 3.13: $\Delta\phi(x)$ versus x . The solid curve is for the second-order approximation, dots correspond to the full FFM. Parameter values are $\gamma = 5 \times 10^{-3}$, $L = 10^6$, $\omega = 1$, and $A = 0.5$.

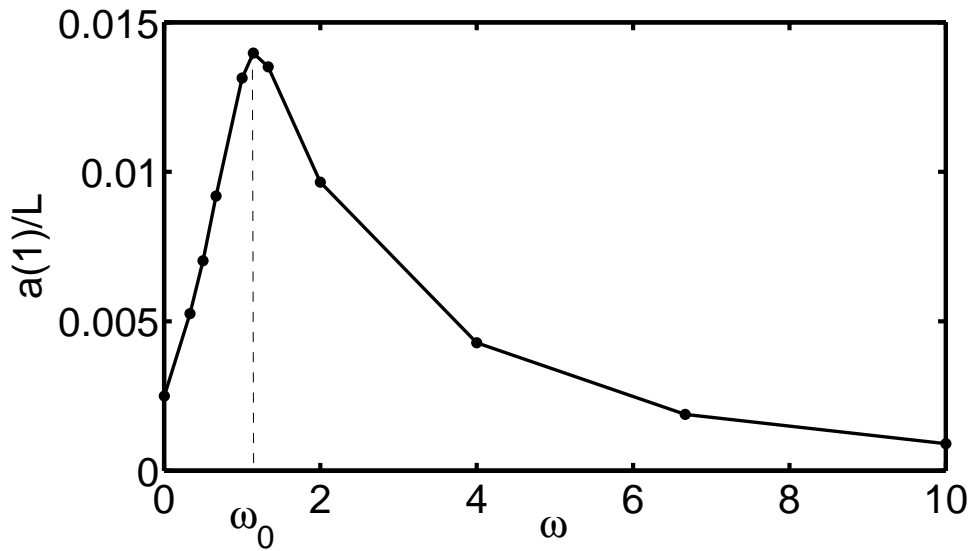


Figure 3.14: $a(1)/L$ versus ω for the second-order approximation ($\omega_0 \approx 1.14$). Parameter values are $\gamma = 5 \times 10^{-3}$, $L = 10^6$, and $A = 0.5$.

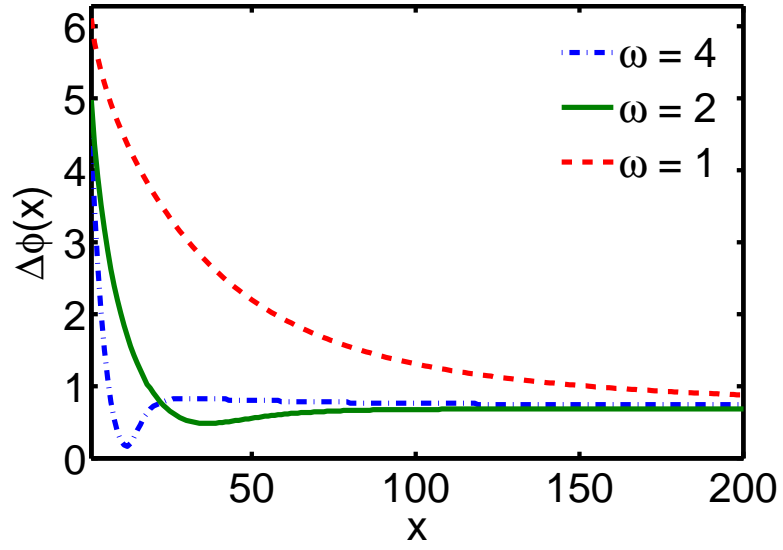


Figure 3.15: $\Delta\phi(x)$ versus x for the second-order approximation. Parameter values are $\gamma_0 = 5 \times 10^{-3}$, $L = 10^6$, $\omega = 1, 2, 4$, and $A = 0.5$.

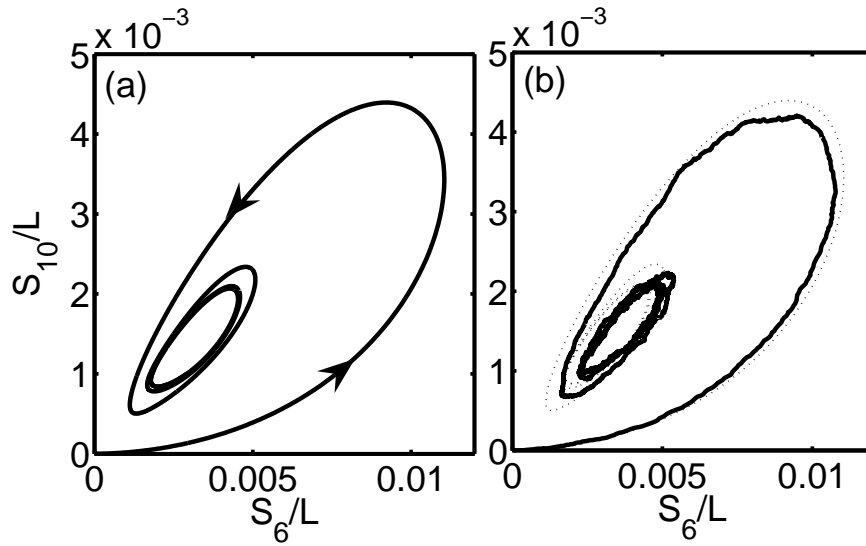


Figure 3.16: S_{10} versus S_6 for $\gamma_0 = 5 \times 10^{-3}$, $L = 10^6$, $\omega = 1$, and $A = 0.5$ for the second order approximation (a) and the FFM (b). The dotted curve in (b) corresponds to the second order approximation.

Chapter 4

Mean-field theory of a recurrent epidemiological model

4.1 Introduction

The effect of social connectivity structure on the behavior of infectious diseases [57] has been of great interest. An important goal of epidemiology is to reveal the connection between the network structure of social connections, the spreading rate of the disease, and the possibility of large epidemic outbreaks [58] [59]. In particular, the degree distribution P_k , defined as the fraction of individuals having k connections to other individuals, is a key factor in determining the properties of epidemic spreading. A signature of epidemiological models is the presence of phase transitions, i.e., qualitative changes in behavior, as the degree distribution or spreading rate is changed [58] [59]. For the intensively studied susceptible-infected-susceptible (SIS) and susceptible-infected-recovered (SIR) epidemiological models, the phase transitions between prevalence and extinction of the disease can be analytically understood, for instance, by using methods of percolation theory [59]. Surprising consequence of these results is the lack of an epidemic threshold [60] and virtually instantaneous spread of the disease [61] for heavy tailed degree distributions.

The purpose of the present Chapter is to provide both analytical and numerical results on the discrete time-step susceptible-infected-recovered-susceptible (SIRS) network model [62]. In particular, our aim is to reveal the connection between

model behavior and the underlying network structure. The SIRS model applies to diseases where individuals cannot obtain permanent resistance against the disease as a result of frequent mutations of the pathogen, e.g., influenza. The discrete time-step approach is justified because, on one hand, it is an approximation to the continuous time case, while on the other hand, our every day life has a certain periodicity, e.g., seasonal changes. For the discrete time-step SIRS model Kuperman *et al.* [62] illustrated the importance of network structure by implementing the model in the Watts-Strogatz framework [63]. It was found that for a regular network, (i.e., a topological ring, where each node has a fixed coordination number), the stationary state of the system is a stable fixed point. As network connections are rewired and random network structure is approached, the fixed point becomes unstable leading to the appearance of self-sustained oscillations. It was also conjectured that on uncorrelated networks the model leads to oscillatory behavior in most cases. In [64] the effect of community structure on the synchronization properties of the SIRS model was studied numerically. The presence of oscillatory states makes the SIRS model particularly interesting, as it provides an example of synchronization phenomena on networks. Qualitatively, similar phase transitions can be observed, for instance, in the well-known Kuramoto model [65].

To account for adaptive behavior in social interactions, recent work [66] proposed a model where the connection structure of the network and the disease itself evolve simultaneously in time. Using adaptive connection structure, susceptible individuals are able to avoid contact with infected ones by rewiring their network connections. Adaptive rewiring leads to regions of bistability, where either a preva-

lent, disease-free, or oscillatory phase can exist as illustrated for both SIR [66] and SIRS models [67].

In a previous theoretical work on the SIRS model, Girvan, *et al.* [68] applied Cooke's discrete time-delay analysis [69] to model epidemics. Synchronization between coupled communities was examined in [70].

In the present Chapter, as an extension of previous numerical [62] and theoretical [68] work, we investigate the discrete time-step SIRS model on uncorrelated networks with arbitrary degree distributions and provide analytical and numerical results on the role of time delays, infection rate, and network structure. We intend to provide a better theoretical basis for the numerous simulation results [62][64]. It is demonstrated that the role of applied contagion scheme is of primary importance and that the model exhibits rich dynamical behavior, with oscillating solutions and fixed points. In particular, the contagion scheme determines the connection between network structure and model behavior. Moreover, while our theoretical results apply for an annealed case, assuming a well mixed population, we find good agreement with the numerical simulations for a fixed network structure, provided the average connectivity of the network is sufficiently large.

The outline of the Chapter is the following. In Sec. II, we provide a framework for the following theoretical discussion. In Sec. III. and Sec. IV, we examine the analytical properties of the two most commonly used contagion schemes. In Sec. V, we compare the obtained results with numerical simulations of the model on a network with fixed connection structure. Finally, in Sec. V we summarize our results and give conclusions.

4.2 Framework

We study a model of infectious disease that has three stages: susceptible S , infected I , and recovered R [62]. Each individual of the population is represented by a node of the network categorized into one of these three stages. Interactions between elements of the population are described by the network connections, and infection can proceed through them. Each element i in the network is characterized by a discrete time counter $\tau_i = 0, 1, \dots, \tau_I + \tau_R$, describing the phase of the disease. Movement between the classes is governed by the following rules. A susceptible (S) element i , whose time counter is by definition $\tau_i = 0$, can become infected if connected to an infected (I) individual. Once infected, the node deterministically goes through a cycle that lasts $\tau_I + \tau_R$ time-steps. In the first τ_I time-steps i is infected and can transmit the disease to its susceptible neighbors. In the following τ_R time-steps, infected individuals pass to the recovered state (R) where individuals are not contagious and are also immune to the disease. The cycle is finally completed when individuals return to the susceptible state and their time counter is set to zero.

Our next step is to specify how infection spreads from an infected to a susceptible individual along network connections. In the present paper we consider two scenarios for disease contagion. The motivation behind this is that the given framework can be applied to a variety of situations, e.g., epidemic dynamics in the human population or computer virus spreading on networks. It is a realistic assumption that local interaction structure in these cases can be quite different. It is essential to understand both the common features and differences arising from implementing

different spreading schemes.

For definition of contagion schemes [62], we consider a susceptible node with connectivity k and k_{inf} infected neighbors. Furthermore, we assume that infection probability can be characterized by a positive spreading rate $0 < \mu \leq 1$. In the first scenario, which is referred to as linear, the probability that the susceptible node becomes infected in a single time-step is $\mu k_{inf}/k$. Specifically, a node becomes infected with probability μ if all of its neighbors are infected. (Previous work [62] for this scheme does not involve the parameter μ , which is equivalent to taking $\mu = 1$.) In the second scenario, referred to nonlinear, we assume that each infected node spreads the disease to its susceptible neighbors with probability μ . Thus, the probability of infection of the susceptible node by its infected neighbors at a given time-step is $1 - (1 - \mu)^{k_{inf}}$.

The time dependence of network structure is a crucial problem that needs to be addressed. Within the framework of uncorrelated networks, we can visualize two fundamentally different approaches. One possibility is when the network connections are fixed in time. This situation is relevant when the timescale of disease spreading is much faster than the timescale that characterizes the creation and destruction of new network connections. This situation, for instance, can describe the spread of computer viruses on the internet. Another option is to consider annealed connection structure, i.e., the network connections are randomly rewired in every time-step, while keeping the coordination number of each node constant. This assumption is justified if the social interaction structure of the population is dominated by random encounters. In reality, every person has a number of fixed connections, e.g., family

members, colleagues, but also interacts randomly with the rest of the population, e.g., while using public transportation. Connectivity of an individual characterizes both fixed connections and random interactions, where in the annealed approach the latter is assumed to be more significant.

In the following theoretical discussion we use annealed approach, assuming that random encounters dominate. While the annealed network structure is meaningful in itself, it also provides a mean-field approximation to the fixed case. In Sec V. we will show that the differences arising from these two approaches disappear, provided that the average connectivity of the network is larger than a threshold.

Every uncorrelated network can be fully characterized by its degree distribution P_k , where P_k is the fraction of nodes with connectivity k . The state of the system is updated in discrete time-steps. In each time-step a fraction of susceptible individuals can become infected. The fraction of nodes that have connectivity k and become infected at time-step t is denoted $i_k(t)$. As each infected individual spends exactly τ_I time-steps in the infected state, and τ_R time-steps in the recovered state, the number of infected, recovered, and susceptible nodes with connectivity k , denoted I_k , R_k , and S_k respectively, equals

$$I_k(t) = \sum_{t'=0}^{\tau_I-1} i_k(t-t'), \quad (4.1)$$

$$R_k(t) = \sum_{t'=\tau_I}^{\tau_I+\tau_R-1} i_k(t-t'), \quad (4.2)$$

$$S_k(t) = P_k - I_k - R_k = P_k - \sum_{t'=0}^{\tau_I+\tau_R-1} i_k(t-t'). \quad (4.3)$$

By definition of uncorrelated networks, when we follow a randomly chosen edge to

one of its endpoints, the probability that we get to node with connectivity k is simply $kP_k/\langle k \rangle$, independent of the node the edge started from. Here we used the notation $\langle k \rangle = \sum_h hP_h$. This is an expression of the fact that high-degree vertices have more edges attached to them than low-degree ones. In annealed networks, infected nodes also form an uncorrelated network, which implies that, if one follows a randomly chosen edge to one of its endpoints, then the probability that the chosen edge goes to an infected node with connectivity k is $kI_k(t)/\langle k \rangle$. For convenience, we introduce the following notations,

$$\langle k \rangle_i(t) = \sum_k k i_k(t), \quad (4.4)$$

$$\langle k \rangle_I(t) = \sum_k k I_k(t) = \sum_{t'=0}^{\tau_I-1} \langle k \rangle_i(t-t'). \quad (4.5)$$

Thus, $\langle k \rangle_i(t)$ is the average degree of nodes that first become infected at time t and $\langle k \rangle_I(t)$ is the average degree the population of all nodes in the infected state at time t . Obviously we have $\langle k \rangle_i(t) \leq \langle k \rangle_I(t)$ and $\langle k \rangle_I(t) \leq \langle k \rangle$. The probability that a given endpoint of a random edge is connected to an infected neighbor,

$$q(t) = \sum_k k I_k(t)/\langle k \rangle = \langle k \rangle_I(t)/\langle k \rangle. \quad (4.6)$$

The probability that a node with connectivity k has exactly x infected neighbors is given by the binomial distribution

$$\binom{k}{x} q(t)^x (1-q(t))^{k-x}. \quad (4.7)$$

If a susceptible node has exactly x infected neighbors, then the probability of infection is by definition $\mu x/k$ in the linear and $1 - (1 - \mu)^x$ in the nonlinear case.

Taking the expectation value of $\mu x/k$ with respect to the above defined binomial distribution yields the result that a susceptible node with connectivity k is infected with probability $\mu q(t)$ in one time-step. For the nonlinear contagion scheme this probability is $1 - (1 - \mu q(t))^k$. We can now formulate our discrete time dynamical equations. The fraction of nodes infected at time-step $t + 1$ equals the fraction of susceptible nodes multiplied by the probability of infection,

$$i_k(t + 1) = \mu \frac{\langle k \rangle_I(t)}{\langle k \rangle} S_k(t), \quad (4.8)$$

for the linear contagion scheme, and

$$i_k(t + 1) = \left(1 - \left(1 - \mu \frac{\langle k \rangle_I(t)}{\langle k \rangle} \right)^k \right) S_k(t), \quad (4.9)$$

for the nonlinear contagion scheme, where $\langle k \rangle_I(t)$ and $S_k(t)$ are given by Eqs. (4.3) and (4.5). Equations (4.8-4.9) define discrete dynamical systems for the variables $i_k(t)$. Note that if $\langle k \rangle$ diverges then the disease disappears after at most $\tau_I + \tau_R$ steps. It is also worth noting that if only one connectivity is present in the degree distribution, i.e., $P[k] = \delta_{k,k_0}$ for some k_0 , and we choose $\tau_I = 1, \tau_R = 0$, then Eq. (4.8) simplifies to the logistic map. Equations (4.8) and (4.9), similarly to the logistic map, show chaotic behavior in certain parameter regions, period doubling etc. Here, however, we restrict our attention to study the transition from fixed point solutions to time-dependent solutions.

In the present Chapter, our main interest is to understand the interplay between network structure and the statistically steady state of the disease. From this perspective, we distinguish three qualitatively different long time scenarios: (i) The disease can die out, resulting in every node becoming susceptible; (ii) the disease

can become prevalent resulting in the average number of infected individuals becoming constant in time; or (iii), the disease can become prevalent with sustained oscillations. The first two scenarios correspond to fixed points of the maps (4.8-4.9), trivial $i_k(t) = 0$ and non trivial $i_k(t) > 0$ respectively, while oscillating solutions are characterized by the instability of both fixed points.

In the following two sections, we examine the existence and the linear stability of solutions for both contagion schemes. The boundary that encompasses the stability regions of the two fixed points will be a curve, where the system undergoes a Neimark-bifurcation.

4.3 Linear contagion scheme

4.3.1 Fixed Points

Our purpose is to understand how the degree distribution (P_k), time delays (τ_I, τ_R), and infection probability μ affect the stability of prevalent, extinct, and oscillating solutions of the discrete dynamical system (4.8). The first step in the following analysis is to determine the fixed points corresponding to the map (4.8). Insertion of Eqs.(4.1) and (4.3) into Eq.(4.8) yields,

$$i_k(t+1) = \mu \frac{\sum_{t'=0}^{\tau_I-1} \langle k \rangle_i(t-t')}{\langle k \rangle} \left(P_k - \sum_{t'=0}^{\tau_I+\tau_R-1} i_k(t-t') \right), \quad (4.10)$$

where $\langle k \rangle_i(t) = \sum_h h i_k(t)$. Fixed points of the system, denoted i_k^* , are time-independent and fulfil the equation,

$$i_k^* = \frac{\mu \tau_I \langle k \rangle_i^*}{\langle k \rangle} [P_k - (\tau_R + \tau_I) i_k^*]. \quad (4.11)$$

The trivial solution $i_k^* = 0$ always exists and is the only solution if the infection rate μ equals zero. We have the self-consistency relation,

$$\langle k \rangle_i^* = \sum_k k i_k^* = \frac{\mu \tau_I \langle k \rangle \langle k \rangle_i^*}{\langle k \rangle + \mu (\tau_I + \tau_R) \tau_I \langle k \rangle_i^*}, \quad (4.12)$$

which for $\langle k \rangle_i^* \neq 0$ can be solved explicitly to yield,

$$\langle k \rangle_i^* = \frac{\langle k \rangle}{\tau_I + \tau_R} \left(1 - \frac{1}{\mu \tau_I} \right), \quad (4.13)$$

$$i_k^* = \frac{P_k}{\tau_I + \tau_R} \left(1 - \frac{1}{\mu \tau_I} \right). \quad (4.14)$$

According to Eqs.(4.13) and (4.14) the distribution of infected nodes is proportional to P_k . I_k and S_k are related to i_k^* via the relationships $I_k = \tau_I i_k^*$ and $R_k = \tau_I i_k^*$. Furthermore, because both i_k^* and $\langle k \rangle_i^*$ are necessarily positive quantities, for $0 \leq \mu \leq 1/\tau_I$, only the trivial ($i_k^* = 0$) solution exists. The critical infection probability, denoted μ_0 , marks the epidemic threshold of the disease, and it is independent of network parameters,

$$\mu_0 = 1/\tau_I. \quad (4.15)$$

Since for $\mu > \mu_0$ both solutions exist and could be stable simultaneously, stability analysis is required to determine the system's behavior. Linear stability of the fixed points can be obtained by adding a small perturbation, $i_k(t) = i_k^* + \delta i_k(t)$, and neglecting terms beyond linear order,

$$\delta i_k(t+1) = \mu \frac{P_k - (\tau_I + \tau_R) i_k^*}{\langle k \rangle} \sum_{t'=0}^{\tau_I-1} \delta \langle k \rangle_i(t-t') - \frac{\mu \tau_I \langle k \rangle_i^*}{\langle k \rangle} \sum_{t'=0}^{\tau_I+\tau_R-1} \delta i_k(t-t'). \quad (4.16)$$

Due to the presence of the terms $\delta\langle k\rangle_i(t-r)$, Eqs. (4.16) are not independent. The analysis, however, can be considerably simplified if we multiply both sides by k and sum over k ,

$$\begin{aligned} \delta\langle k\rangle_i(t+1) = \mu \frac{\langle k\rangle - (\tau_I + \tau_R) \langle k\rangle_i^*}{\langle k\rangle} \sum_{t'=0}^{\tau_I-1} \delta\langle k\rangle_i(t-t') \\ - \frac{\mu\tau_I \langle k\rangle_i^*}{\langle k\rangle} \sum_{t'=0}^{\tau_I+\tau_R-1} \delta\langle k\rangle_i(t-t'). \end{aligned} \quad (4.17)$$

With the notation

$$a = \mu - \mu(\tau_I + \tau_R) \langle k\rangle_i^* / \langle k\rangle, \quad (4.18)$$

$$b = -\mu\tau_I \langle k\rangle_i^* / \langle k\rangle, \quad (4.19)$$

and $x_t = \delta\langle k\rangle_i(t)$ we can rewrite Eq.(4.17),

$$x_{t+1} = a \sum_{t'=0}^{\tau_I-1} x_{t-t'} + b \sum_{t'=0}^{\tau_I+\tau_R-1} x_{t-t'}, \quad (4.20)$$

where $a = \mu$ and $b = 0$ for the trivial and $a = 1/\tau_I$ and $b = -(\mu\tau_I - 1)/(\tau_I + \tau_R)$ for the non-trivial solution given by Eqs. (4.13) and (4.14). Surprisingly, both a and b are independent of P_k . As a result, stability of the fixed points is determined only by the time delays τ_I, τ_R and μ . Hence, for linear contagion the underlying network structure is unimportant, in contrast with the nonlinear scheme, where the role of degree distribution is essential, as we will see in Sec V.

4.3.2 Shur Stability

Equation (4.20) defines a linear $\tau_I + \tau_R$ -dimensional discrete time dynamical system. We devote some time to examine its stability properties for arbitrary a and

b , because the general results obtained will be used in the rest of the Chapter. In order to determine the a, b pairs, where the linear system (4.20) is stable we look for eigen-solutions of Eq.(4.17), in the form, $x_t = x_0 \lambda^t$ for complex λ , leading to the algebraic equation

$$\lambda = a \sum_{r=0}^{\tau_I-1} \lambda^{-r} + b \sum_{r=0}^{\tau_I+\tau_R-1} \lambda^{-r}. \quad (4.21)$$

The dynamical system (4.20) is stable if all roots of the polynomial (4.21) have absolute value smaller than one. Since $a \geq 0$ and $b \leq 0$, we can restrict our attention to the lower right quarter of the (a, b) plane. Possible boundaries between stability and instability can be determined by looking for solutions of Eq. (4.21) on the complex unit circle $\lambda = e^{i\phi}$. If $\phi = 0$, we obtain $1 = \tau_I a + (\tau_I + \tau_R) b$. If, however, $\phi \neq 0$, we can sum the trigonometric series in (4.21) to obtain

$$a(\phi) = \frac{\sin((\tau_I + \tau_R + 1)\phi/2) \sin(\phi/2)}{\sin(\tau_I\phi/2) \sin(\tau_R\phi/2)}, \quad (4.22)$$

$$b(\phi) = -\frac{\sin((\tau_I + 1)\phi/2) \sin(\phi/2)}{\sin((\tau_I + \tau_R)\phi/2) \sin(\tau_R\phi/2)}. \quad (4.23)$$

Equations (4.22) and (4.23) for $0 \leq \phi \leq 2\pi$ represent a discontinuous curve that divides the (a, b) plane into stable and unstable regions. At this point, however, we do not know which of these regions correspond to stable (a, b) pairs. An analytical solution to this problem can be worked out, using Shur's theorem [72] as given in Appendix B. Also see [73]. Here, we omit this part and determine the nature of the relevant regions numerically. Stability regions of Eq. (4.20) in the lower right quarter plane are shown in Fig. 4.1. The curves encompassing the region of stability can be easily identified. The line corresponds to $1 = \tau_I a + (\tau_I + \tau_R) b$, while the

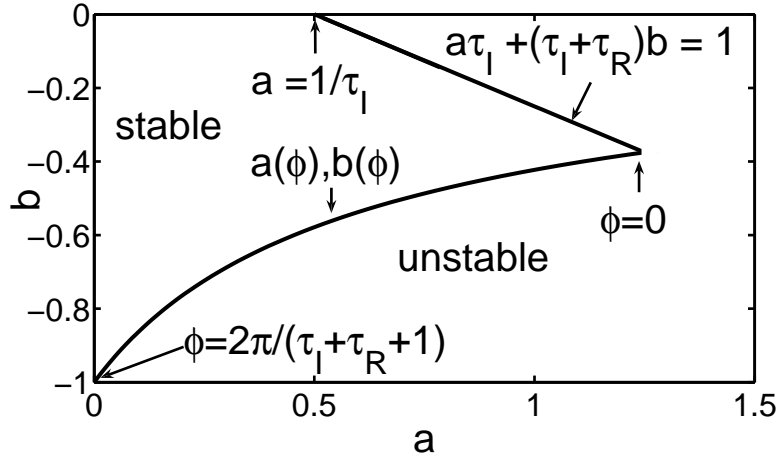


Figure 4.1: Stability regions for Eq.(4.21) for $\tau_I = 2$ and $\tau_R = 2$. The straight line starting from point $(a, b) = (1/\tau_I, 0)$ corresponds to the equation $a\tau_I + b(\tau_I + \tau_R) = 1$, while the curve is given by Eqs. (4.22) and (4.23).

curve starting at the point $(a, b) = (0, -1)$ is given by $\phi \rightarrow (a(\phi), b(\phi))$, as defined in Eqs. (4.22) and (4.23). The parametric curve intersects the $1 = \tau_I a + (\tau_I + \tau_R) b$ line at $\phi = 0$ and the $a = 0$ axis at $\phi = 2\pi/(\tau_I + \tau_R + 1)$.

4.3.3 Phase Diagram

As the line $a\tau_I + b(\tau_I + \tau_R) = 1$ intersects the $b = 0$ axis at $a = 1/\tau_I$, the stability criterion for the trivial solution ($a = \mu, b = 0$) is $a = \mu < 1/\tau_I = \mu_0$, i.e., the trivial fixed point is unstable whenever the non-zero solution exists. A remarkable feature of this critical point is that it is determined exclusively by τ_I . For the nontrivial solution (4.13-4.14), on the other hand, we have $a = 1/\tau_I, b = -(\mu\tau_I - 1)/(\tau_I + \tau_R)$, which defines a vertical line starting at $a = 1/\tau_I$ as shown in Fig. 4.2. The critical value of μ where this line intersects the unstable region, denoted μ_1 , marks the Neimark-bifurcation point where oscillating solutions emerge. If $\mu_1 > 1$ for fixed τ_I and τ_R , then oscillations do not occur. We can obtain a simple approximation for

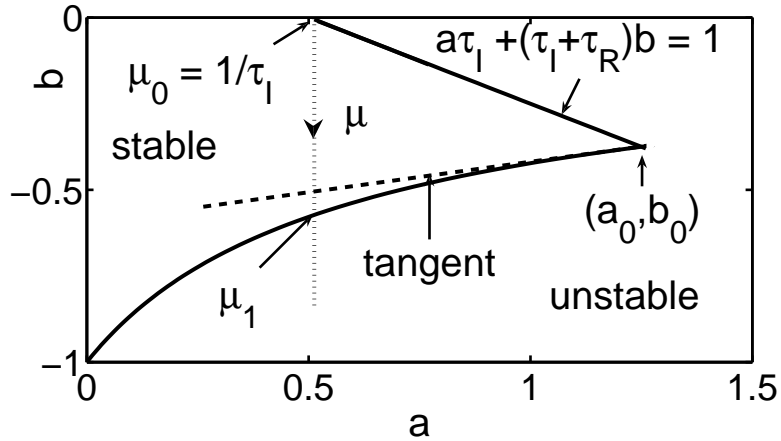


Figure 4.2: Approximation of the border of stability region with a tangent starting at point (a_0, b_0) , for $\tau_I = 2$ and $\tau_R = 2$.

μ_1 by taking the tangent of the parametric curve at $\phi = 0$, point (a_0, b_0) as shown in Fig. 4.2, and calculating μ where this tangent intersects the line given by $a = 1/\tau_I$ and $b = -(\mu\tau_I - 1)/(\tau_I + \tau_R)$. A simple calculation yields,

$$\frac{\mu_1 - \mu_0}{\mu_0} \approx \frac{2(\tau_I + 1)}{\tau_R + 1}, \text{ for } \tau_R > \tau_I \text{ and } \mu_0 = \frac{1}{\tau_I}. \quad (4.24)$$

Details of the derivation are discussed in Appendix C. We note that the accuracy of Eq.(4.24) improves with increasing τ_R and it provides an excellent approximate value for μ_1 . A simple consequence of Eq.(4.24) is that μ_1 converges to $\mu_0 = 1/\tau_I$ as $\tau_R \rightarrow \infty$, and for large τ_R the region where prevalence exists without oscillations disappears.

We summarize our results in Fig. 4.3 for $\tau_I = 4$. Regions corresponding to prevalence, extinction, and oscillatory solutions are shown as functions of μ and τ_R . The solid line separating the oscillatory and prevalent regions represents the full numerical solution of Eqs.(4.17), while the dashed curve approximation (4.24). We find excellent quantitative agreement. The infection rate μ_1 asymptotically

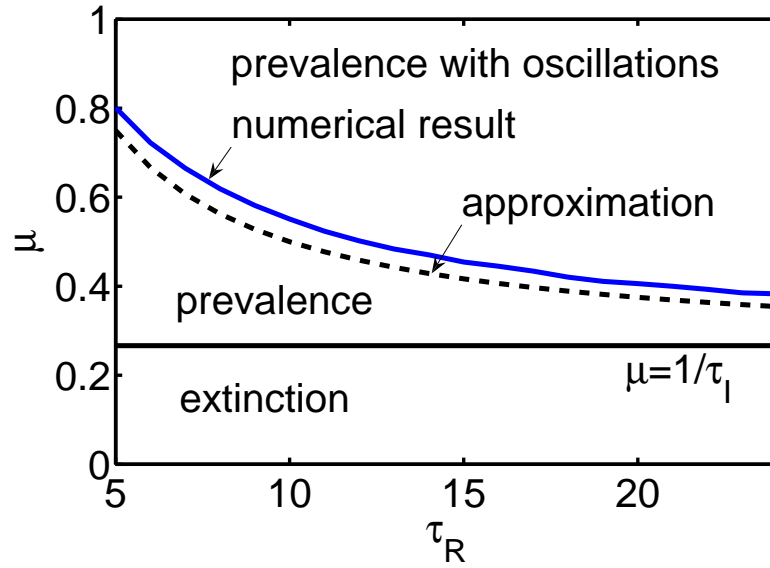


Figure 4.3: Phase portrait of Eq.(4.10) with $\tau_I = 4$. The solid curve separating oscillatory and prevalent solutions is obtained from full numerical solution of Eq.(4.10), while the dotted curve is given by (4.24).

approaches $\mu_0 = 1/\tau_I$. Moreover, if $\tau_I = 2$, then for $\tau_R \leq 4$ we do not have an oscillatory phase for any $\mu \leq 1$. In general, for a given τ_I we need a minimum number of time-steps spent in the recovered phase to observe oscillations, in good agreement with Eq. (4.24).

4.4 Nonlinear scheme

We have seen in the previous section that emergence of prevalent and oscillatory solutions for linear contagion were independent of the degree distribution. Introduction of nonlinearity, however, leads to explicit dependence on the network structure. In this section, we first explore the properties of the non-trivial fixed points, and we then turn to presentation of the analytical characterization of the oscillatory phase.

4.4.1 Fixed Points

The discrete-time dynamical system in this case is given by Eq. (4.9). Its fixed points, denoted i_k^* , must satisfy,

$$i_k^* = P_k \frac{1 - \left(1 - \tau_I \mu \frac{\langle k \rangle_i^*}{\langle k \rangle}\right)^k}{1 + (\tau_I + \tau_R) - (\tau_I + \tau_R) \left(1 - \tau_I \mu \frac{\langle k \rangle_i^*}{\langle k \rangle}\right)^k}. \quad (4.25)$$

Equation (4.25) provides solutions in terms of the parameter $\langle k \rangle_i^*$. With the introduction of $f(x)$,

$$f(x) = \sum_h \frac{h P_h \left(1 - \left(1 - \tau_I \mu \frac{x}{\langle k \rangle}\right)^h\right)}{1 + (\tau_I + \tau_R) - (\tau_I + \tau_R) \left(1 - \tau_I \mu \frac{x}{\langle k \rangle}\right)^h}, \quad (4.26)$$

the self-consistency requirement, $\sum_h h i_k^* = \langle k \rangle_i^*$, is equivalent to the fixed point problem $f(x_*) = x_*$, where $x_* = \langle k \rangle_i^*$ as shown in Fig. 4.4. $f(0) = 0$ is always satisfied, and, for $x_{\max} \equiv \langle k \rangle / \mu \tau_I$, we have the inequality,

$$f(x_{\max}) = \frac{\langle k \rangle}{\tau_I + \tau_R + 1} < x_{\max}, \quad (4.27)$$

Furthermore, because $f(x)$ is concave ($f'' < 0$), $f(x)$ intersects the x line at a point $x > 0$ if and only if $f'(0) > 1$, yielding the existence condition $f'(0) = \mu \tau_I \langle k^2 \rangle / \langle k \rangle \geq 1$. As a result, for a given degree distribution we obtain the epidemic threshold,

$$\mu_0 = \frac{\langle k \rangle}{\tau_I \langle k^2 \rangle}. \quad (4.28)$$

Equation (4.28) agrees with the result obtained for the SIR model [60], if we choose specifically $\tau_I = 1$. An important consequence of Eq. (4.28) is that for divergent $\langle k^2 \rangle$ we get $\mu_0 = 0$, e.g., for a power law degree distribution $P_k \sim k^{-\gamma}$, with exponent $\gamma < 3$, any non-zero infection probability leads to an epidemic

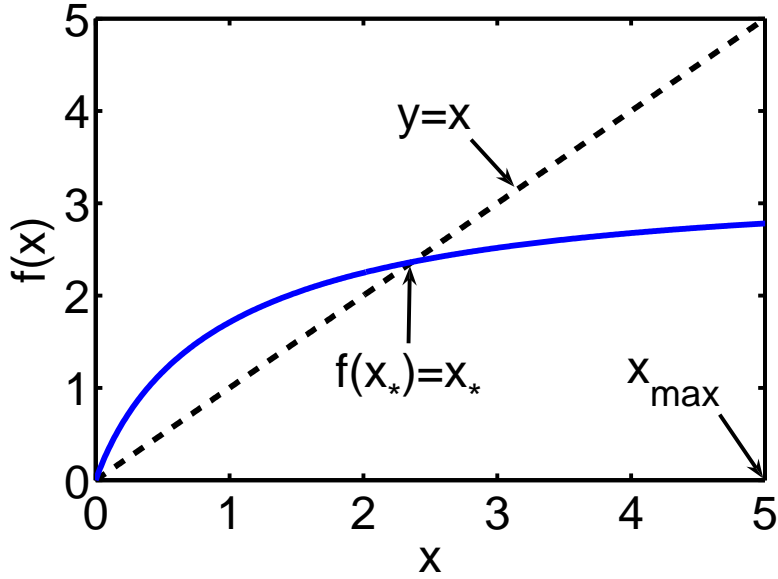


Figure 4.4: Solution of the fixed point problem $x = f(x)$, where $f(x)$ is given by Eq.(4.26).

outbreak, provided that the network has infinitely many nodes. Since the non-zero fixed point $f(x_*) = x_*$ is attractive ($f'(x_*) < 1$), successive application of the map for any $x_0 \neq 0$ converges to the solution, $x_* = \lim_{n \rightarrow \infty} f^n(x_0)$. It is easy to see that $\langle k \rangle_i^*$ is an increasing function of μ (its derivative is given explicitly in Appendix C.) and, under conditions discussed below, it asymptotically approaches $\langle k \rangle_i^{\max} = \langle k \rangle / (\tau_R + \tau_I + 1)$. Indeed, this asymptotic behavior is valid if $|x - f(x)|_{\mu=1} \ll 1$ at $x = \langle k \rangle / (\tau_R + \tau_I + 1)$. Using the explicit form of $f(x)$ this condition is satisfied if $\sum_h h P_h (\tau_R / (\tau_R + \tau_I))^h \ll \langle k \rangle$.

Motivated by the results of the linear case (4.13), we approximate $\langle k \rangle_i^*$ with $\langle k \rangle_i^* \simeq a + b/\mu$, which, considering the asymptotic behavior of $\langle k \rangle_i^*$ and the condition $\langle k \rangle_i^*|_{\mu=\mu_0} = 0$, yields,

$$\langle k \rangle_i^* \simeq \frac{\langle k \rangle}{\tau_I + \tau_R + 1} \left(1 - \frac{\mu_0}{\mu} \right) \frac{1}{1 - \mu_0}, \text{ for } \mu \geq \mu_0. \quad (4.29)$$

We will not provide rigorous proof of Eq. (4.29), but note that it agrees with the exact solution within 5% provided $\sum_h hP_h (\tau_R/(\tau_R + \tau_I))^h \ll \langle k \rangle$. Accordingly, the fraction of infected individuals can be approximated by

$$I^* \simeq \frac{\tau_I}{\tau_I + \tau_R + 1} \left(1 - \frac{\mu_0}{\mu}\right) \frac{1}{1 - \mu_0}, \text{ for } \mu \geq \mu_0. \quad (4.30)$$

We will compare (4.30) with experimental results in Sec. V.

4.4.2 Stability

After obtaining existence condition for the time-independent solutions of the discrete time dynamical equations we now turn to examine their stability. Adding a small perturbation to i_k^* , i.e., $i_k(t) = i_k^* + \delta i_k(t)$, and neglecting terms beyond linear order yields,

$$\delta i_k(t+1) = \left(\sum_{t'=0}^{\tau_I-1} \delta \langle k \rangle_i(t-t') \right) a_k - b_k \sum_{t'=0}^{\tau_I+\tau_R-1} \delta i_k(t-t'). \quad (4.31)$$

where,

$$a_k = \frac{k\mu}{\langle k \rangle} (P_k - (\tau_I + \tau_R) i_k^*) \left(1 - \tau_I \mu \frac{\langle k \rangle_i^*}{\langle k \rangle}\right)^{k-1}, \quad (4.32)$$

$$b_k = 1 - \left(1 - \tau_I \mu \frac{\langle k \rangle_i^*}{\langle k \rangle}\right)^k. \quad (4.33)$$

An important difference between Eq.(4.31) and Eq. (4.17) is that b_k 's depend explicitly on the coordination number k , and, unless $P_k = \delta_{k,k_0}$ for some k_0 , we cannot handle the problem analytically in its full generality. Nevertheless, the trivial case ($\langle k \rangle_i^* = 0$) can be solved exactly. If $\langle k \rangle_i^* = 0$, then Eq.(4.31) yields,

$$\delta i_k(t+1) = \left(\sum_{r=0}^{\tau_I-1} \delta \langle k \rangle_i(t-r) \right) \frac{k\mu}{\langle k \rangle} P_k, \quad (4.34)$$

Multiplying both sides by k and summing, we obtain

$$\delta\langle k \rangle_i(t+1) = \left(\sum_{r=0}^{\tau_I-1} \delta\langle k \rangle_i(t-r) \right) \frac{\langle k^2 \rangle \mu}{\langle k \rangle}, \quad (4.35)$$

which is Eq. (4.20) with $b = 0$ and $a = \mu\langle k^2 \rangle / \langle k \rangle$. As discussed in Sec. III.A, the condition for stability in this case is $a = \mu\langle k^2 \rangle / \langle k \rangle < 1/\tau_I$, or equivalently $\mu < \mu_0$.

Therefore, the trivial fixed point is unstable whenever the non-zero solution exists.

If $\delta i_k(t) \neq 0$, then we look for eigen-solutions of Eq.(4.31) in the form $\delta i_k(t) = r_k \lambda^t$.

Substitution of $\delta i_k(t) = r_k \lambda^t$ into (4.31) yields,

$$r_k = \frac{a_k \sum_h h r_h}{\lambda + b_k \sum_{r=0}^{\tau_I-1} \lambda^{-r}} \sum_{r=0}^{\tau_I+\tau_R-1} \lambda^{-r}, \quad (4.36)$$

Multiplying both sides of Eq.(4.36) with k and summing, leads to the self-consistency relation,

$$1 = \sum_h \frac{h a_h}{\lambda + b_h \sum_{r=0}^{\tau_I+\tau_R-1} \lambda^{-r}} \sum_{r=0}^{\tau_I-1} \lambda^{-r}. \quad (4.37)$$

In particular, the system is stable if all λ solutions of (4.37) lie inside the complex unit cycle. Since $b_k = 0$ at $\mu = \mu_0$ for all k , we can obtain a perturbative solution of Eq. (4.37) for $\mu - \mu_0 \ll 1$, $b_k \ll 1$, as follows. For $b_k = 0$ we obtain the zeroth-order expression,

$$\frac{\lambda}{\sum_h h a_h} = \sum_{r=0}^{\tau_I-1} \lambda^{-r}, \quad (4.38)$$

If $b_k \approx 0$, we take the first-order approximation of the quotient in Eq.(4.37), i.e.,

$1 / (1 + b_h \sum_{r=0}^{\tau_I+\tau_R-1} \lambda^{-r-1}) \simeq 1 - b_h \sum_{r=0}^{\tau_I+\tau_R-1} \lambda^{-r-1}$, to obtain,

$$\lambda = \sum_h h a_h \sum_{r=0}^{\tau_I-1} \lambda^{-r} - \sum_h h a_h b_h \sum_{r=0}^{\tau_I+\tau_R-1} \lambda^{-r} \sum_{r=0}^{\tau_I-1} \lambda^{-r-1}. \quad (4.39)$$

Finally, we replace the sum $\sum_{r=0}^{\tau_I-1} \lambda^{-r-1}$ in the second (perturbative) term with (4.38),

$$\lambda = \sum_h h a_h \sum_{r=0}^{\tau_I-1} \lambda^{-r} - \frac{\sum_h h a_h b_h}{\sum_h h a_h} \sum_{r=0}^{\tau_I+\tau_R-1} \lambda^{-r}. \quad (4.40)$$

Note that, Eq. (4.40) is exact if $P_k = \delta_{k,k_0}$ for some k_0 . Introducing the notation $a = \sum_h h a_h$ and $b = \sum_h h a_h b_h / \sum_h h a_h$, the polynomial (4.40) corresponds exactly to Eq. (4.21), and therefore the results obtained for its stability in Sec. III can be applied. Since for $\mu - \mu_0 \ll 1$ we have $b_k \sim k(\mu - \mu_0)$, we can expect Eq.(4.40) to be a good approximation if the network has few highly connected nodes. We also find that the accuracy of (4.40) improves with increasing τ_R . We have $a = 1/\tau_I$ and $b = 0$ at $\mu = \mu_0$, independently of the degree distribution, and the curve $\mu \rightarrow (a(\mu), b(\mu))$ intersects the $b = 0$ axis with a tangent $db/da = 2\tau_I$, see Appendix C. The infection probability where the curve $\mu \rightarrow (a(\mu), b(\mu))$ enters the instability region of Eq. (4.40) is the Neimark-bifurcation point μ_1 . For $\mu - \mu_0 \ll 1$, we can substitute a and b with their first-order Taylor-expansion (given in the Appendix C) and follow the same argument that lead to Eq. (4.24), (i.e., approximating the boundary of instability with a line), leading to

$$\frac{\mu_1 - \mu_0}{\mu_0} \simeq \frac{2(\tau_I + 1)(\tau_I + \tau_R)}{\tau_R(\tau_I + \tau_R - \tau_I^2/2)}, \quad (4.41)$$

where μ_0 is given by Eq.(4.28). In the $\tau_R \gg \tau_I$ limit,

$$\frac{\mu_1 - \mu_0}{\mu_0} \approx \frac{2(\tau_I + 1)}{\tau_R} \text{ as } \tau_R \rightarrow \infty. \quad (4.42)$$

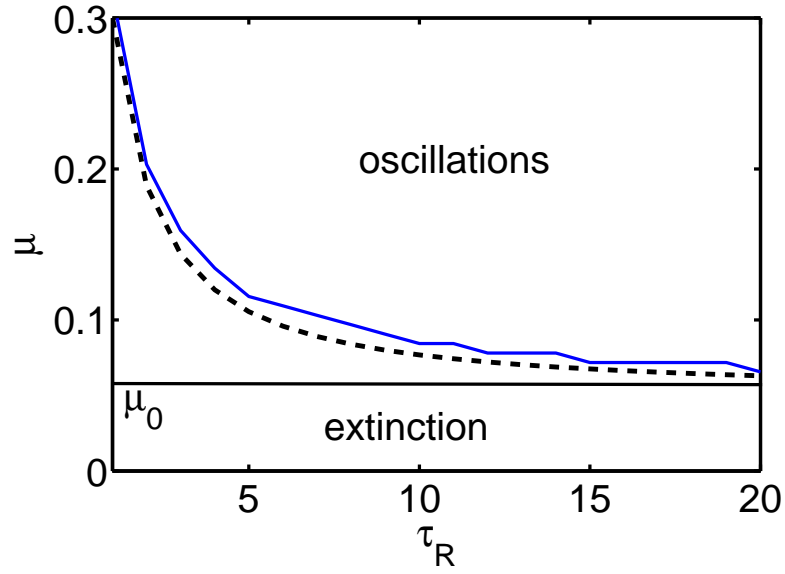


Figure 4.5: Stability regions for the nonlinear scheme as a function of τ_R and infection probability μ for $\tau_I = 2$. Results for the full numerical simulation (solid curve) are compared to the approximation corresponding to Eq. (4.41) (dashed curve) for the degree distribution $P_k = \delta_{k,10}$.

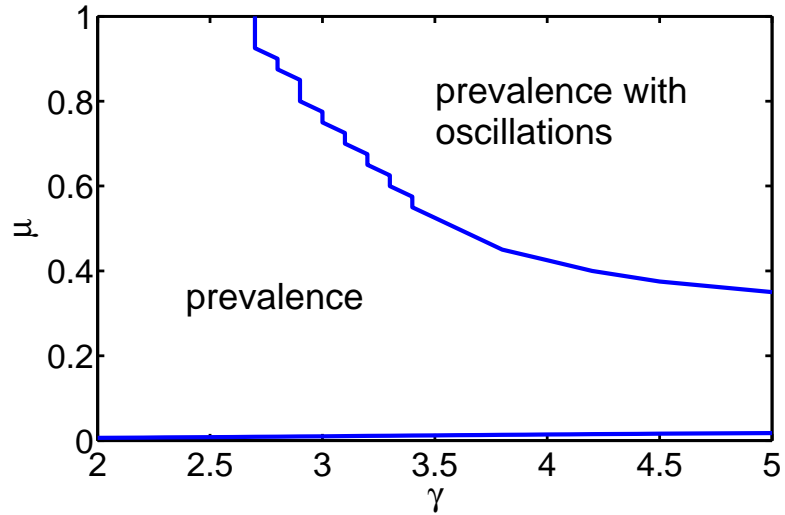


Figure 4.6: Stability regions for nonlinear contagion obtained from full numerical solution of Eqs.(4.31), with $P_k \sim k^{-\gamma}$, $\tau_I = 4$, and $\tau_R = 2$.

Asymptotically, we obtain the same behavior as in the linear case (4.24). However, for small τ_R there is a significant difference between these two systems. Figure 4.5 shows the stability regions for the nonlinear contagion scheme for $P_k = \delta_{k,10}$ and $\tau_I = 2$. The solid line separating oscillating and fixed point solutions is obtained from the full numerical solution of Eqs. (4.31), while the dashed curve is given by Eq. (4.41). We find excellent agreement. However, for $\tau_I > \tau_R$, from numerical simulations we find that Eq. (4.41) does not provide accurate results. Therefore, in this case we chose to determine the occurrence instability numerically. Qualitatively, the reason for this inaccuracy is that for $\tau_I > \tau_R$ we have $\mu_1 \gg \mu_0$, and first-order Taylor-expansion of a and b will no longer provide reliable results. Figure 4.6 shows regions of stability obtained for a power law degree distribution with variable exponent γ , i.e., $P_k \sim k^{-\gamma}$, for $\tau_I = 4$ and $\tau_R = 2$. We applied an upper cutoff of P_k at $k = 100$. The phase portrait is shown as a function of the exponent γ and infection probability, revealing strong dependence on γ , in particular, oscillations are completely absent if γ falls below a critical value. We find that this behavior is typical of fat tailed distributions and can also be observed for $P_k \sim e^{-\alpha k}$ if $\alpha < 0.1$. We note that the numerical solution of Eq. (4.31) requires extra attention when $\mu \simeq 1$, because in this region the system is marginally stable, and usually a large number of time-steps are necessary to determine the stability properties of the fixed point, (on the order of 10^6).

4.5 Numerical results for fixed network structure

To assess how well our annealed results apply to a fixed network structure, we implemented the SIRS model on a network consisting of 1.5×10^4 nodes for both contagion schemes. Each node on the network was initialized randomly in either a susceptible, infected, or recovered state. The time counter of the infected and refractory nodes was also set randomly between $1, \dots, \tau_I$ and τ_I, \dots, τ_R respectively. After initialization, we waited 8×10^3 time-steps to allow the transients related to initial conditions to relax. If we denote the time counter of a node k by τ_k ($\tau_k \in 0, \dots, \tau_I + \tau_R$) and the number of nodes by N , then emergence of oscillations can be well characterized by the synchronization parameter [65]-[62],

$$\sigma(t) = \left| \frac{1}{N} \sum_k e^{\tau_k 2\pi i / (\tau_I + \tau_R)} \right|, \quad (4.43)$$

where the sum is taken over all nodes of the network except the susceptible ones ($\tau_k = 0$). The appearance of persistent oscillations corresponds to synchronization of elements in the system. Their phases, τ_k , in the epidemic cycle become synchronized as the disease process proceeds. This synchronization is captured by $\sigma(t)$, which plays the role of an order parameter [62]. After transients relax, we calculate $\sigma(t)$ averaged over 200 realizations taken over a period of 2×10^3 time-steps.

4.5.1 Linear Contagion

For linear contagion, we demonstrate that the obtained results are independent of the degree distribution, as suggested by our annealed theory. On the other hand, we evaluate how accurately our analytical considerations predict the phase

transitions between extinction and prevalence (4.13,4.14) and the fixed point solution and oscillatory phase (4.24). For a given network structure, we fix $\tau_I = 4$ and we run a series of simulations for different τ_R and P_k . We find that the higher the average coordination number of the network $\langle k \rangle$, the better the agreement between our mean field results and numerical simulations. In general, $\langle k \rangle \geq 15$ provides excellent correspondence between theory and experiment. Similarly, increasing τ_R improves the reliability of our mean field results. We argue that the reason for this is that recovered elements in the network do not interact. The longer the recovered stage, the fewer individuals are active (susceptible or infected) at a given time instant, making the network effectively sparse. Thus, large τ_R has a tendency to diminish correlations, leading to mean-field behavior. By contrast, for $\tau_I > \tau_R$ correlations are expected to have more of an effect.

We generate uncorrelated networks for the degree distributions $P_k \sim \delta_{k,10}$, $P_k \sim \delta_{k,15}$, $P_k \sim e^{-0.1k}$, and $P_k \sim k^{-3}$. For both the exponential and the power-law cases we take $P_k = 0$ for $k < 10$ and $k > 100$. We applied the cutoff for large connectivities to limit finite size effects. Figure 4.7 shows σ versus μ for two distinct distributions. The solid curve corresponds to an exponential distribution, while the dashed to a power-law distribution. Apparently, the curves are almost identical, supporting the mean field result. Figure 4.8 compares the number of infected individuals as a function of infection rate for the mean field approximation (4.13-4.14) (solid curve) and numerical simulations (dashed curve). Again we find excellent agreement. Most importantly, the theoretical epidemic threshold, $\mu = 1/\tau_I$, agrees very well with our numerical results. Figure 4.9 compares μ_1 (Neimark-

bifurcation point) for the mean field results with the experiments for $P_k = \delta_{k,10}$ (dotted curve) and $P_k = \delta_{k,15}$ (dashed curve) versus the time-delay τ_R . Figure 4.9 illustrates that with increasing $\langle k \rangle$ we approach the mean field results.

4.5.2 Nonlinear Contagion

For nonlinear contagion, we first verify that the approximation given in Eq.(4.30) accurately gives the fraction of infected nodes. Figure 4.10 compares the experimental results (dashed curve) with the formula (4.30) for $\tau_I = 1$, $\tau_R = 4$, and $P_k \sim k^{-4}$, indicating good agreement. Figure 4.11 compares the experimental results for a fixed network structure with numerical solution of the annealed mean field equations (4.31) for μ_1 (Neimark-bifurcation point). The curves are almost identical. However, if $\tau_I > \tau_R$, the mean field approximation does not agree well with our numerical simulations. We conjecture that this can be attributed to the increased presence of correlations. While the epidemic threshold is still well characterized by (4.28), for the Neimark-bifurcation (μ_1) displays considerable disagreement between the annealed theory and the fixed network simulation. Figure 4.12 shows numerical results for μ_1 and a fixed network structure with $\tau_I = 4$, $\tau_R = 2$, and $P_k \sim k^{-\gamma}$ for variable exponent. Comparison of Fig. 4.6 and Figure 4.12 reveals, unlike in mean field theory, for a fixed network structure, small γ promotes oscillations.

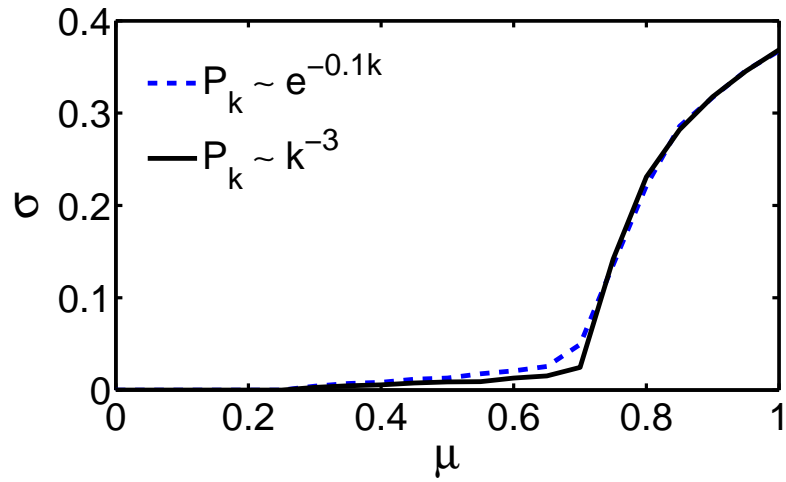


Figure 4.7: Comparison of experimental results of σ with distributions $P_k \sim e^{-0.1k}$ and $P_k \sim k^{-3}$ for $\tau_I = 4$, $\tau_R = 7$, and $N = 1.5 \times 10^4$. (Linear contagion)

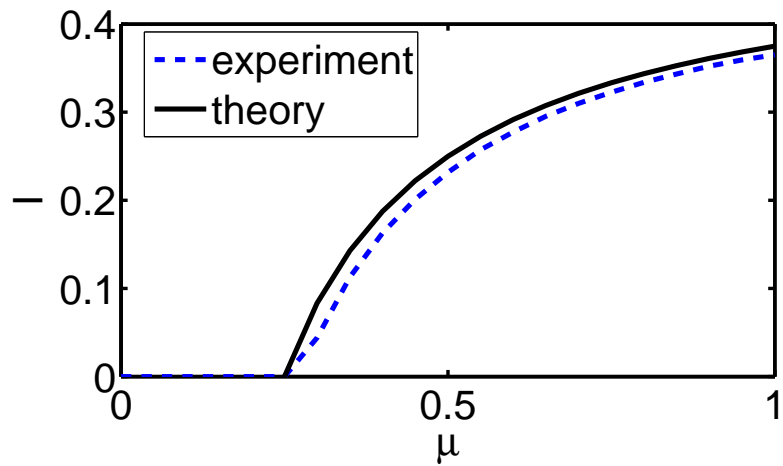


Figure 4.8: Comparison of experimental (dashed curve) and mean-field results (4.13-4.14) (continuous curve) for the fraction of infected individuals (I) for $\tau_I = 4$, $\tau_R = 4$, $P_k \sim e^{-0.1k}$, and $N = 1.5 \times 10^4$. (Linear contagion)

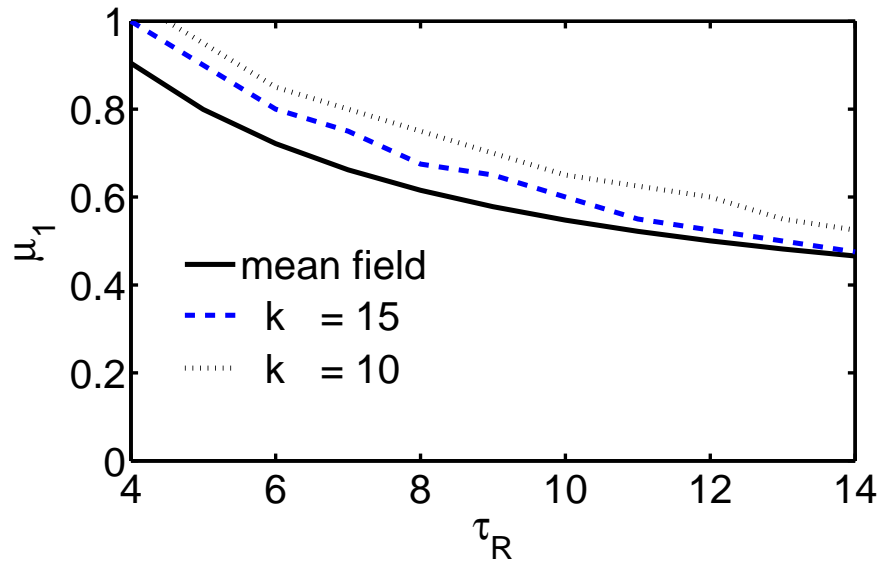


Figure 4.9: Comparison of mean-field results (4.24) (continuous curve) with experimental results for the Neimark-bifurcation point μ_1 as function of τ_R for the distributions $P_k = \delta_{k,15}$ (dashed curve) and $P_k = \delta_{k,10}$ (dotted curve) for $\tau_I = 4$ and $N = 1.5 \times 10^4$. (Linear contagion)

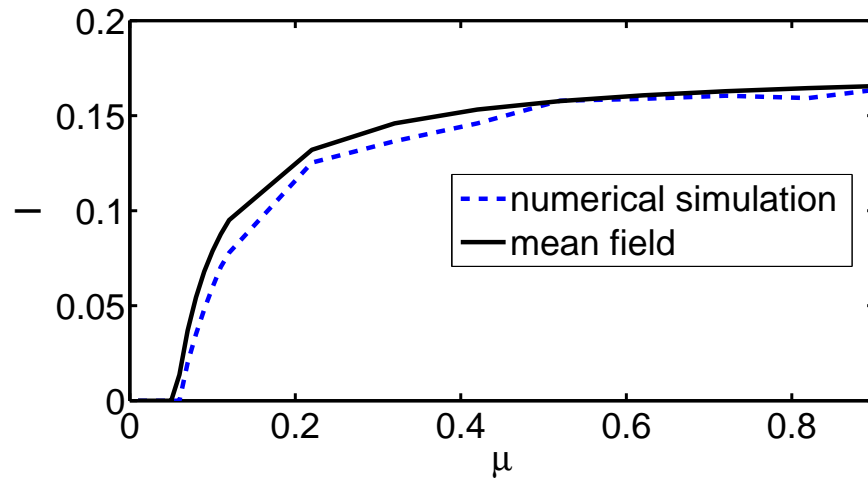


Figure 4.10: Comparison of experimental (dashed curve) and mean-field results (4.30) (continuous curve) for the fraction of infected individuals (I), for $\tau_I = 1$, $\tau_R = 4$, $P_k \sim k^{-4}$, and $N = 1.5 \times 10^4$. (Nonlinear contagion)

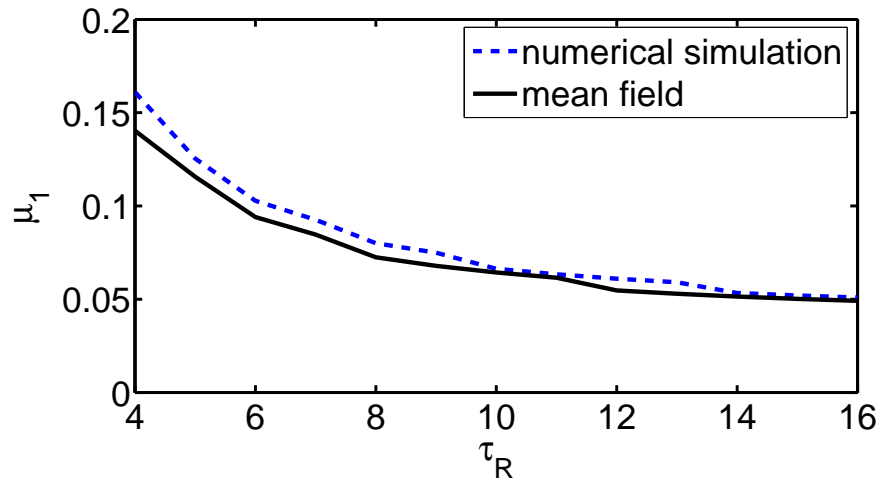


Figure 4.11: Comparison of mean-field results (4.24) (continuous curve) with experimental results (dashed curve) for the Neimark-bifurcation point μ_1 as function of τ_R . $P_k \sim k^{-4}$, $\tau_I = 2$, $\tau_R = 4$ and $N = 1.5 \times 10^4$. (Nonlinear case)

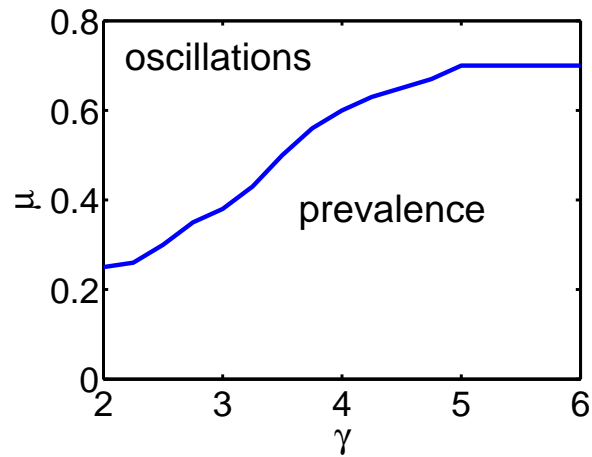


Figure 4.12: Experimental results for the for the Neimark-bifurcation point μ_1 , for $P_k \sim k^{-\gamma}$ as function of the exponent γ , $\tau_I = 4$, $\tau_R = 2$, and $N = 2 \times 10^4$.

4.6 Conclusion

In this Chapter we have developed a mean field theory for the discrete time-step SIRS model for the two most commonly studied contagion schemes. We found that for linear contagion the stability of prevalent, extinct, and oscillatory solutions is independent of the network structure, and the model behavior is determined exclusively by the time-delays and infection probability. Numerical simulations for a fixed network structure were in excellent agreement with our theoretical predictions. By contrast, for the nonlinear contagion scheme, the epidemic threshold (μ_0) and occurrence of Neimark-bifurcation (μ_1) depend strongly on the underlying network. However, the asymptotic behavior of the dimensionless quantity $(\mu_1 - \mu_0) / \mu_0$, is the same for both schemes as $\tau_R \rightarrow \infty$, Eqs.(4.24) and (4.41). We also found that the importance of the degree distribution is even more pronounced if the duration of infected stage exceeds τ_R , i.e., $\tau_I > \tau_R$. Referring to Fig. 4.6 we see that oscillations can be completely absent for power-law degree distributions with small exponents. In the case $\tau_I > \tau_R$, however, predictions of mean field theory do not agree well with numerical simulations for a fixed network structure. We attribute this fact to correlations, which are not incorporated in the mean field approach. In summary, we have shown that the discrete time SIRS model exhibits rich dynamical behavior even within the framework of uncorrelated networks, and that the contagion scheme, time delays, and infection probability play a vital role in determining model behavior.

4.7 Appendix A

For $L \gg 1$, γ constant and $\gamma \sum_y y^2 S(y, t) \ll 1$ the solution of (3.17) can be given by introducing $F(x, t) = S_x(t)e^{-(2+\gamma x)t}$,

$$\frac{dF(x, t)}{dt} = \frac{e^{-(2-\gamma)t}}{N_e(t)} \sum_{a+b+1=x} F(a, t)F(b, t). \quad (4.44)$$

Equation (4.44) can be explicitly solved for the generating function $G(z, t) = \sum_{y=0}^L z^y F(y, t)$,

$$G(z, t) = \frac{G(z, 0)}{1 - zG(z, 0) \int_0^t e^{-(2-\gamma)\tau} / N_e(\tau) d\tau}. \quad (4.45)$$

In particular for empty grid initial condition, (i.e., $G(z, 0) = L$), Eq. (4.45) yields

$$S_x(t) = L \left(\frac{1 - e^{-(1-\gamma)t}}{1 - \gamma} \right)^x e^{-(2+\gamma x)t}, \quad (4.46)$$

$$N_e(t) = Le^{-t}.$$

Accordingly, t_{\max} , defined in Sec. 3.3 ($dS_x(t_{\max})/dt = 0$), can be approximated as

$$t_{\max}(x) \approx \ln \left(\frac{x}{2} + 1 \right), \quad (4.47)$$

and the the magnitude of the first maximum is

$$S_{\max}(x) = S_x(t_{\max}) \approx \frac{4x^x}{(x+2)^{x+2}}. \quad (4.48)$$

4.8 Appendix B

The asymptotic stability of the polynomial (4.21) is strongly connected to Shur's theorem [72]. A polynomial is stable if all of its roots have absolute value smaller than one. In general, it is possible to associate a characteristic polynomial

$$w(z) = a_0 z^n + \dots + a_{n-1} z + a_n \quad (4.49)$$

with the symmetric matrix $P = S_1^T S_1 - S_2^T S_2$ where

$$S_1 = \begin{pmatrix} a_0 & \dots & a_{n-2} & a_{n-1} \\ 0 & \ddots & \vdots & a_{n-2} \\ \vdots & & \ddots & \vdots \\ 0 & 0 & 0 & a_0 \end{pmatrix}, S_2 = \begin{pmatrix} a_n & \dots & a_{n-1} & a_1 \\ 0 & \ddots & \vdots & a_2 \\ \vdots & & \ddots & \vdots \\ 0 & 0 & 0 & a_n \end{pmatrix}.$$

The polynomial $w(z)$ is asymptotically stable if and only if the matrix P is positive definite. According to Sylvester's criterion this requirement is satisfied if all determinants associated with the upper left sub-matrices are positive, providing us an analytical approach to determine the stability regions of Eq.(4.21) as polynomials of a and b . If we denote the n -th upper left sub-determinant of P with p_n , then for a given (a, b) pair $\det(p_n) > 0$ for all n is a necessary and sufficient condition for stability. The curves corresponding to Eqs. (4.22-4.23) are given by $\det(p_n) = 0$.

4.9 Appendix C

The location where the two instability curves intersect is given by (a_0, b_0) in Fig.4.2. This position can be calculated by taking the $\phi \rightarrow 0$ limit of the expressions (4.22-4.23),

$$a_0 = \lim_{\phi \rightarrow 0} a(\phi) = \frac{\tau_I + \tau_R + 1}{\tau_I \tau_R},$$

$$b_0 = \lim_{\phi \rightarrow 0} b(\phi) = -\frac{\tau_I + 1}{\tau_R (\tau_I + \tau_R)}.$$

The derivative $db/da|_{\phi=0}$ is most easily evaluated using a symbolic mathematical software package,

$$\left. \frac{db}{da} \right|_{\phi=0} = \left. \frac{db/d\phi}{da/d\phi} \right|_{\phi=0} = \tau_I \frac{\tau_R - 1}{(\tau_I + \tau_R)(\tau_R + 1)}.$$

For the nonlinear contagion scheme Taylor-expansion of $\sum_h ha_h$ and $\sum_h ha_h b_h$ with respect to the parameter μ yields,

$$a = \sum_h ha_h \simeq \frac{1}{\tau_I} + \frac{\mu - \mu_0}{\mu_0} \frac{\tau_I}{(\tau_I + \tau_R)}, \quad (4.50)$$

$$b = \sum_h ha_h b_h \simeq -\frac{\mu - \mu_0}{\mu_0} \frac{2\tau_I}{\tau_I + \tau_R}. \quad (4.51)$$

To obtain formulas (4.50-4.51) we used the identity

$$\left. \frac{d\langle k \rangle_i^*}{d\mu} \right|_{\mu=\mu_0} = \frac{\tau_I}{\tau_I + \tau_R} \frac{\langle k^2 \rangle^3}{\langle k \rangle \langle k^3 \rangle}, \quad (4.52)$$

which is a consequence of Eq. (4.37).

Bibliography

- [1] S. Albeviro, V. Jentsch and H. Kantz, editors, *Extreme Events in Nature and Society* (Springer Verlag, 2006).
- [2] A.R. Osborne, M. Onorato, and M. Serio, *Phys. Lett. A* **275**, 386 (2000).
- [3] E.J. Boettcher, J. Fineberg, and D.P. Lathrop, *Phys. Rev. Lett.* **85**, 2030 (2000).
- [4] D. Battogtokh and A. Mikhailov, *Physica D* **90**, 84 (1996); **106**, 327 (1997).
- [5] R.J. Wiener, D.C. Dolby, G.C. Gibbs, B. Squires, T. Olsen, and A.M. Smiley, *Phys. Rev. Lett.* **83**, 2340 (1999).
- [6] W. Lu, D. Yu, and R.G. Harrison, *Phys. Rev. Lett.* **76**, 3316 (1996); **78** 4375 (1997).
- [7] R. Roy, T.W. Murphy, T.D. Maier, Z. Gills, and E.R. Hunt, *Phys. Rev. Lett.* **68**, 1259 (1992).
- [8] E. Ott, C. Grebogi, and J. A. Yorke, *Phys. Rev. Lett.* **64**, 1196 (1990).
- [9] K. Pyragas, *Phys. Lett. A* **170**, 2265 (1992).
- [10] H. Gang and Q. Zhilin, *Phys. Rev. Lett.* **72**, 68 (1994).
- [11] R.O. Grigoriev, M.C. Cross, and H.G. Schuster, *Phys. Rev. Lett.* **79**, 2795 (1997).
- [12] C. Grebogi, E. Ott and J.A. Yorke, *Physica D* **7**, 181 (1983).
- [13] W. Yang, M. Ding, A. Mandell and E. Ott, *Phys. Rev. E* **51**, 102 (1995); V. In, M.L. Spano, J.D. Neff, W.L. Ditto, S. Daw, K.D. Edwards and K. Nyguen, *Chaos* **7**, 605 (1997). Although these papers consider the suppression of a boundary crisis event, they also clearly apply directly to suppression of intermittent bursts (i.e., ‘rare intense events’) associated with interior crises [12].
- [14] J. Katz, *Physics Today* **60**, 13 (July, 2007); K. Emanuel, *ibid.*; R. Simpson and J. Simpson, *Trans. NY Acad. Sci.* **28**, 1045 (1966)

- [15] T. Bohr, M.H. Jensen, A. Vulpiani and G. Paladin, *Dynamical Systems Approach to Turbulence*, Chapter 5 (Cambridge, Cambridge University Press, 2005).
- [16] A.C. Newell and J.A. Whitehead, *J. Fluid Mech.* **38**, 279 (1969).
- [17] G. Ahlers and D.S. Cannell, *Phys. Rev. Lett.* **50**, 1583, (1983).
- [18] K. Stewartson and J.T. Stuart, *J. Fluid Mech.* **48**, 529, (1971).
- [19] Y. Kuramoto, *Chemical Oscillations, Waves and Turbulence* (Series in Synergetics Vol. 19 Springer, New York, 1984).
- [20] M. Bartuccelli, J.D. Gibbon, and M. Oliver, *Physica D* **89**, 267 (1996).
- [21] A. Mileke, *Physica D* **117**, 106 (1998).
- [22] M. Gabbay, E. Ott and P.N. Guzdar, *Physica D* **118**, 371 (1998); Sect.3.
- [23] M.J. Landman, G.C. Papanicolaou, C. Sulem and P.L. Sulem, *Phys. Rev. A* **38**, 3837 (1988).
- [24] B.J. LeMersurrier, G.C. Papanicolau, C. Sulem, and P.L. Sulem, *Physica D* **32**, 210 (1988).
- [25] G. Fibich and G.C. Papanicolaou, *Phys. Lett. A* **239**, 167 (1998).
- [26] C.D. Levermore and D. R. Stark, *Phys. Let. A* **234**, 269 (1997).
- [27] R.E. Wilson, *Physica D* **112**, 329 (1997).
- [28] B. P. Luce and C. R. Doering, *Phys. Lett. A* **178**, 92 (1993).
- [29] G. Fibich and D. Levy, *Phys. Lett. A* **249**, 286 (1998).
- [30] F. Merle and P. Raphael, *Comm. Math Physics* **253**, 675 (2005).
- [31] F. Merle and P. Raphael, *Invent. Math.* **156**, 565 (2004).
- [32] J.W. Kim and E. Ott, *Phys. Rev. E* **67**, 026203 (2003).

- [33] In addition to control by modifying an intrinsic parameter of the system (e.g., our discussion of changing the parameter α), one might also envision adding an *externally applied* ‘control force’ $f(x,t)$ to the right hand side of (2.1) with the intrinsic system unchanged. We note, however, that our changing of α can also be viewed as an external force control with $f(x,t)$ chosen to be $i\alpha(\alpha'(x,t) - \alpha)|u|^2 u$. Other choices for the control force $f(x,t)$ might, e.g., utilize an added nonlinear dissipation (such as $-m(x,t)|u|^\sigma u$ with $\sigma = 2, 3, \dots$) or an added dispersion (such as $ip(x,t)\nabla^{2n}u$ with $n = 1, 2, \dots$). We have tried some of these alternative forms for the control, and found that they can also perform well when used in our forecast driven control scenario illustrated in Figs. 2.5- 2.6.
- [34] A. Doleman and E.S. Titi, Num. Func. Anal. and Opt. **14**, 299 (1993).
- [35] R. Montagne, P. Colet, Phys. Rev. E **56**, 4017 (1997).
- [36] L. Junge and U. Parlitz, Phys. Rev. E **61**, 3736 (2000).
- [37] S. Boccaletti, J. Bragard, and F. T. Arecchi, Phys. Rev. E **59**, 6574 (1999).
- [38] P. Bak, C. Tang, and K. Wiesenfeld, Phys. Lett. **59**, 381 (1987); Phys. Rev. A. **38**, 364 (1988).
- [39] L. P. Kadanoff, S. R. Nagel, L. Wu, and S.M. Zhou, Phys. Rev. A **39**, 6524 (1989).
- [40] D. Dhar, Phys. Rev. Lett. **64**, 1613 (1990).
- [41] Z. Olami, H.J.S. Feder, and K. Christensen, Phys. Rev. Lett. **68**, 1244 (1992).
- [42] T.A. Witten and L.M. Sander, Phys. Rev. Lett. **47**, 1400 (1981).
- [43] D. Wilkinson and J.F. Willemsen, J. Phys. A **16**, 3365 (1983).
- [44] M. Paczuski, S. Boettcher, and M. Baiesi, Phys. Rev. Lett. **95**, 181102 (2005).
- [45] P. Bak, K. Chen and C. Tang, Phys. Lett. A **147**, 297 (1990).
- [46] B. Drossel and F. Schwabl, Phys. Rev. Lett. **69**, 1629 (1992).
- [47] P. Grassberger, J. Phys. A **26**, 2081 (1993).
- [48] B. Drossel, Phys. Rev. Lett. **76**, 936 (1996).

- [49] B. Drossel, S. Clar, and F. Schwabl Phys. Rev. Lett. **71**, 3739 (1993).
- [50] K. Christensen, H. Flyvbjerg, and Zeev Olami, Phys. Rev. Lett. **71**, 2737 (1993).
- [51] D.L. Turcotte, B.D. Malamud, G. Morein, W.I. Newman Physica A **268**, 629 (1999).
- [52] V. Loreto, L. Pietronero, A. Vespignani, and S. Zapperi, Phys. Rev. Lett. **75**, 465 (1995).
- [53] A.-L. Barabasi and R. Albert, Science **286**, 509 (1999).
- [54] M. Paczuski and P. Bak, Phys. Rev. E **48**, R3214 (1993).
- [55] A. Honecker and I. Peschel, Physica A **239**, 509 (1997).
- [56] S. Clar, B. Drossel, and F. Schwabl, J. Phys. Condens. Matter **8**, 6803 (1996).
- [57] R. M. Anderson and R. M. May, *Infectious Diseases of Humans*. (Oxford University Press, 1991).
- [58] R. Pastor-Satorras and A. Vespignani, Phys. Rev. Lett. **86**, 3200 (2001).
- [59] M. E. J. Newman Phys. Rev. E **66**, 016128 (2002).
- [60] Y. Moreno, R. Pastor-Satorras, and A. Vespignani, European Physical Journal B **26**, 521-529 (2002).
- [61] M. Barthelemy, A. Barrat, R. Pastor-Satorras, A. Vespignani, Phys Rev Lett. **92**, 178701 (2004).
- [62] M. Kuperman and G. Abramson, Phys. Rev. Lett. **86**, 2909 (2001)
- [63] D.J. Watts and S.H. Strogatz, Nature **393**, 440 (1998).
- [64] G. Yan, Zhong-Qian Fu, J. Ren, and Wen-Xu Wang, Phys. Rev. E **75**, 016108 (2007).
- [65] Y. Kuramoto, *Chemical Oscillations, Waves, and Turbulence* (Springer, Berlin 1984)

- [66] T. Gross, C.J. Dommar D’Lima, and B. Blasius Phys. Rev. Lett. **96**, 208701 (2006).
- [67] L.B. Shaw and I. B. Schwartz, Phys. Rev. E **77**, 066101, (2008).
- [68] M. Girvan, D.S. Callaway, M.E.J. Newman, and S.H. Strogatz, Phys. Rev. E. **65**, 031915 (2002).
- [69] K. L. Cooke, D.F. Calef, and E.V. Level, *Nonlinear Systems and its Applications*, Academic Press, New York, 73-93 (1977).
- [70] D. He and L. Stone, Proc. R. Soc. Lond. **270**, 1519 (2003).
- [71] Y. Hayashi, M. Minoura, and Jun Matsukubo Phys. Rev. E **69**, 016112 (2004.)
- [72] T. Kaczorek, *Theory of Control and Systems*, PWN (1993); M. Hazewinkel *Encyclopaedia of mathematics*
- [73] We emphasize that the curves given by Eqs. (4.22) and (4.23) are only possible stability boundaries of Eq.(4.20). E.g. if we cross such a curve, one of the eigenvalues typically goes from $|\lambda| < 1$ to $|\lambda| > 1$, but if one of the other eigenvalues already has $|\lambda| > 1$, then there is instability on both sides of the curve.